

Entanglement-Induced Resilience of Quantum Dynamics

Tianfeng Feng,¹ Yue Cao,¹ Wenjun Yu,¹ Junkai Zeng,² Xiaopeng Li,^{3,*} Xiu-Hao Deng,^{2,4,†} and Qi Zhao^{1,2,‡}

¹*QICI Quantum Information and Computation Initiative, Department of Computer Science, The University of Hong Kong, Pokfulam Road, Hong Kong SAR, China*

²*Shenzhen International Quantum Academy, Shenzhen 518048, China*

³*State Key Laboratory of Surface Physics, Key Laboratory of Micro and Nano Photonic Structures (MOE), and Department of Physics, Fudan University, Shanghai 200433, China*

⁴*Shenzhen Branch, Hefei National Laboratory, Shenzhen, 518048, China*

(Dated: February 25, 2026)

Quantum many-body devices suffer from imperfections that destabilize dynamics and limit scalability. We show that the dynamical growth of entanglement can intrinsically protect generic quantum dynamics against coherent and perturbative noise. Through rigorous theoretical analysis of general quantum dynamics and numerical simulations of spin chains and fermionic lattices, we prove that entanglement-entropy growth confines the influence of local Hamiltonian perturbations, thereby suppressing errors in dynamical errors. The degree of protection correlates quantitatively with the entanglement entropy of subsystems on which the perturbations act, and applies broadly to both analog quantum simulators and real-time control protocols. This entanglement-induced resilience is conceptually distinct from quantum error correction or dynamical decoupling: it passively leverages native many-body correlations without additional qubits, measurements, or control overhead. Our results reveal a generic mechanism linking entanglement growth to dynamical stability and provide practical guidelines for designing noise-resilient quantum devices.

Quantum many-body systems hold great promise for advancing technologies ranging from analog quantum simulators to fault-tolerant quantum computers [1–4]. However, a major obstacle limits their practical realization: all real-world systems suffer from imperfections. Static disorder—such as fabrication-induced variations in qubit parameters—may dramatically alter quantum phases [5–8]. Equally problematic is crosstalk between components or control pulse distortions, which creates structured errors that resist conventional error suppression methods [9–12]. These imperfections destabilize quantum dynamics, threatening the scalability of quantum devices. Current solutions like error-correcting codes or dynamical decoupling often require significant overhead [13–15]. This raises a critical question: Can quantum systems naturally exhibit inherent resilience against these coherent or perturbative imperfections without external intervention?

Entanglement is a hallmark of quantum correlations that plays a central role in the dynamics of many-body systems [5, 16–18]. It underpins a broad range of tasks in quantum information processing and quantum computing [19–21]. Recent studies suggest that, in certain regimes, entanglement might play a stabilizing role in simulating quantum systems [22, 23]. In digital quantum simulations [24, 25], the generation of entanglement helps reduce the algorithmic errors caused by the discretization of time evolution (Trotterization) [22]. However, digital quantum simulation remains experimentally challenging, and despite extensive efforts [24–27], a significant

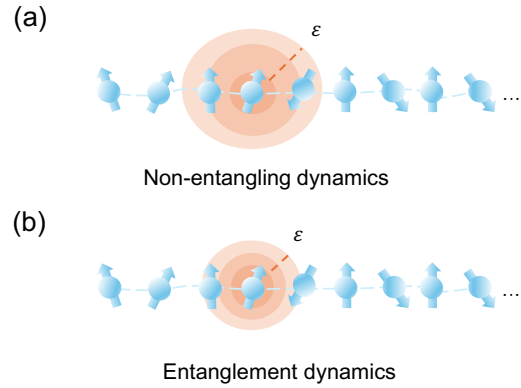


FIG. 1: Entanglement-induced resilience of quantum dynamics. The red shaded band shows the error envelope. Consider a local error Hamiltonian acting on a spin chain, where the error terms involve k near-neighbour qubits and comprise $\text{poly}(k)$ Pauli operators with small coefficients. (a) When the quantum system exhibits weak or no entanglement, the dynamical error may scale linearly with the number of error terms, i.e., $\text{poly}(k)$. (b) In contrast, sufficient entanglement suppresses the dynamical error, leading to a scaling proportional to the square root of the number of error terms, i.e., $\sqrt{\text{poly}(k)}$.

gap persists between current capabilities and the requirements for scalable, fault-tolerant implementations [28]. In contrast, analog simulation provides a promising near-term platform not only for strongly coupled fermionic systems such as the Fermi-Hubbard model [29–32] but also for a variety of other many-body models, including spin models [33, 34], bosonic systems [35, 36], and lattice

* xiaopeng_li@fudan.edu.cn

† dengxiuhao@iqasz.cn

‡ zhaoqi@cs.hku.hk

gauge theories [37–39].

While most analog quantum simulations have traditionally focused on ground-state properties and the characterization of quantum phases, our research emphasizes the (real-time) dynamical behavior of quantum systems and simulators. A fundamental question arises: does entanglement universally enhance robustness in continuous quantum dynamics—such as in analog simulations or real-time control protocols? Specifically, does entanglement passively coexist with reliable dynamics, or does it actively suppress intrinsic dynamical errors? This question is especially pertinent in many-body systems where imperfection and disorder intricately interact with complex spatial-temporal correlations.

In this work, we reveal that the dynamic growth of entanglement provides intrinsic protection against perturbations, including disorder and crosstalk couplings of unitary quantum dynamics. A conceptual overview of our results is presented in Fig. 1, where error accumulation is suppressed through entanglement. By combining analytical models and numerical simulations (spin chains, fermionic lattices), we show that rapidly increasing entanglement entropy confines local perturbations, preventing their spread. This mechanism applies broadly to analog quantum simulations and beyond, where greater entanglement correlates with higher operational fidelity. Furthermore, to bridge the gap between theory and experiment, we introduce a dynamical entanglement detection scheme based on error subspaces. We demonstrate that measuring experimentally accessible correlation functions of the noise terms serves as an effective probe to diagnose whether the dynamics is protected by entanglement, circumventing the need for full quantum state tomography.

Our results reshape the understanding of entanglement’s role in realistic dynamics: while static entanglement is often fragile under local, uncorrelated noise, its dynamic generation in many-body evolution can inherently suppress coherent errors—distinct from engineered quantum error correction. We identify this as a natural error suppression mechanism embedded in many-body quantum dynamics. Practically, these insights offer guidelines for designing robust quantum protocols: intentionally engineering entanglement growth through tailored interactions or control sequences can enhance resilience without additional resources such as extra qubits or syndrome measurements. Furthermore, larger entanglement regions are classically hard to simulate [40, 41], which not only enhances the quantum advantage but also suggests that extensive entanglement can further bolster error suppression and computational power in many-body systems. These findings immediately benefit analog quantum simulators by leveraging native entanglement dynamics to improve robustness without additional error correction [42, 43].

I. ENTANGLEMENT INDUCES DYNAMIC RESILIENCE

Disorders and imperfections in Quantum dynamics.— Errors in quantum dynamics arise from perturbations—imperfections of coupling and disorder—that perturb the real-time evolution of quantum states. These dynamical errors are ubiquitous across platforms, not only in analog quantum simulators but also in digital emulation and real-time control protocols. One can model the perturbed evolution by $H'(t) = H_0(t) + H_{\text{pert}}(t)$, yielding the evolved state $|\psi'(t)\rangle = \mathcal{T}e^{-i \int H'(t)dt} |\psi(0)\rangle$ with \mathcal{T} the time-ordering operator.

Generally, perturbations from stochastic disorder and imperfections are unified under a generalized perturbative Hamiltonian term

$$H_{\text{pert}}(t) = \sum_k \delta_k V_k + \sum_m \eta_m N_m, \quad (1)$$

where δ_k parameterizes random disorder (e.g., pulse distortions in quantum control or lattice potential fluctuations in analog simulations), while $\eta_m N_m$ represents time-invariant noise from systematic errors, such as fabrication-induced variations, residual crosstalk couplings in multi-qubit gates [9] or the effective Trotterization artifacts in digital algorithms [25]). Crucially, disorder and imperfection strength bifurcate dynamical responses: Weak perturbation induces perturbative energy shifts without altering phase topology, as seen in trapped-ion spectral jitter; Strong disorder or imperfection, however, may drive symmetry-breaking or topological phase transitions—MBL shifts entanglement scaling from volume-law to area-law in spin chains [5].

Entanglement-induced resilience of quantum dynamics.— Without loss of generality, we begin with the time-dependent scenario, where the time-independent case can be treated as a special simplification. Suppose $H_0(t)$ is the ideal Hamiltonian and $H'(t)$ is the noisy Hamiltonian with perturbation, the evolution of the ideal and noisy unitaries are given as $U_0(t) = \mathcal{T}e^{-i \int_{s=0}^t ds H_0(s)}$ and $U(t) = \mathcal{T}e^{-i \int_{s=0}^t ds H'(s)}$ respectively. Here, we would like to quantify the distance between $U_0(t)$ and $U(t)$ with initial state $|\psi(0)\rangle$. To explore the role of entanglement in the quantum dynamics, we utilize the vector norm $\|(U_0(t) - U(t))|\psi(0)\rangle\|$ to track the quantum dynamics errors (Here the vector norm is defined as $\|X|\psi\rangle\| = \sqrt{\langle\psi|X^\dagger X|\psi\rangle}$, and the spectral norm $\|X\| = \max_{|\psi\rangle} \|X|\psi\rangle\|$, capturing the worst input state case). It is shown that $W(t) = U(t)^\dagger U_0(t)$ is the unique solution of $i\partial_t W(t) = U(t)^\dagger (H(t) - H'(t))U(t)W(t)$ with $W(0) = I$ [44, 45], by unitary invariant property of vector norm and the triangle inequality, we can bound the dynamic error as (see section A in Materials and Methods)

$$\|(U_0(t) - U(t))|\psi\rangle\| \leq \int_0^t d\tau \| [H'(\tau) - H_0(\tau)] |\psi(\tau)\rangle \|, \quad (2)$$

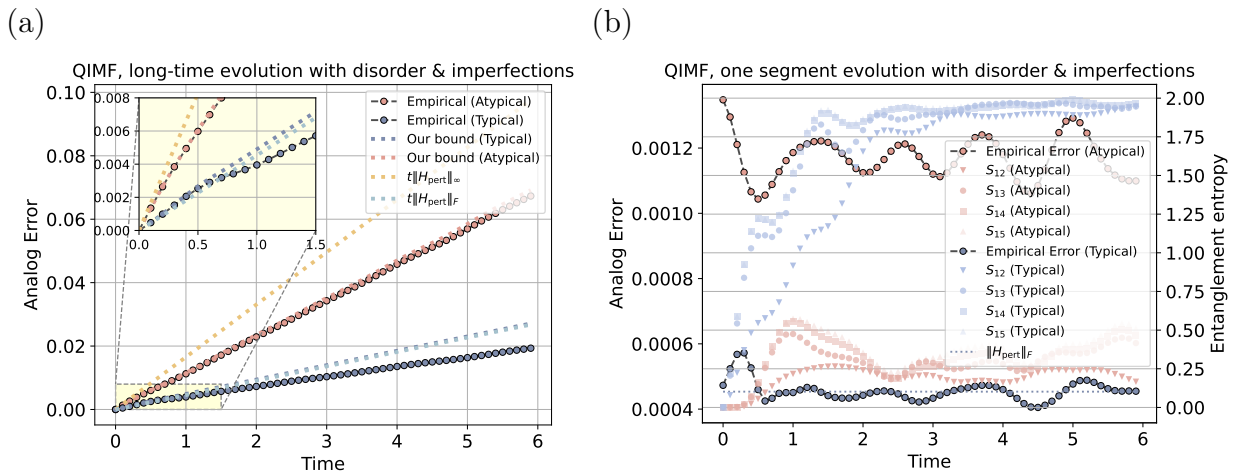


FIG. 2: Error of Analog quantum simulation of 1D QIMF model in typical and atypical cases. The perturbation Hamiltonian is comprised of disorder terms with coefficients $\delta_i \in \mathcal{N}(0, 0.01)$ and an imperfection term $\eta = 0.01$. (a) Long-time analog simulation error. In typical input state, where the entanglement entropy grows during the system's evolution, our estimate closely matches the average-case performance, scaling with $\|H_{\text{pert}}\|_F$. Notably, at early times when entanglement has not yet developed sufficiently, the error curve exhibits a slight curvature with a slope higher than the average-case estimate. However, after the entanglement saturates (around $t \approx 0.5$), the error slope aligns with the average case, and our bound and the average-case bound run approximately parallel. In contrast, in an atypical input state, where the entanglement entropy remains low throughout the evolution, the error scaling deviates significantly from the average case and approaches the worst-case bound characterized by the spectral norm. (b) One-segment simulation error, $\|(U_0(\delta t) - U(\delta t))|\psi(t)\rangle\|_F$, evaluated for different initial states with $\delta t = 0.1$. The corresponding entanglement entropy of two qubits ($S_{1,2}$, $S_{1,3}$, $S_{1,4}$, $S_{1,5}$) is also shown, illustrating how entropy growth correlates with error suppression.

This upper bound on the error is governed by the Hamiltonian mismatch $H'(\tau) - H_0(\tau)$, which in general arises for time-dependent Hamiltonians. Here $|\psi(\tau)\rangle$ denotes the ideally evolved state at time τ . Since the perturbed Hamiltonian can be expressed as $H'(\tau) = H_0(\tau) + H_{\text{pert}}(t)$, The upper bound of the dynamic error now is given as $\int_0^t d\tau \|H_{\text{pert}}(t)|\psi(\tau)\rangle\|$, i.e.,

$$\int_0^t d\tau \sqrt{\langle \psi(\tau) | H_{\text{pert}}^\dagger(t) H_{\text{pert}}(t) | \psi(\tau) \rangle}. \quad (3)$$

This bound can characterize errors in various dynamical processes, including real-time quantum control.

To better characterize this bound, we connect it to the entanglement entropy of the quantum state. For simplicity, here we consider the perturbation H_{pert} to be time-independent and consists of local perturbative terms $H_{\text{pert}} = \sum_j H_{\text{pert},j}$ (We put the time-dependent analysis in Methods.) It is shown that the expectation value of a positive semi-definite operator can be related to the entanglement entropy of a quantum state [22]. Specifically, let $A = \sum_j A_j$ be a positive semi-defined operator, acting on N qubits, where A_j acts nontrivially on the subsystem $\text{supp}(A_j)$, then $|\langle \psi | A | \psi \rangle| \leq \frac{\text{Tr}(A)}{d} + \Delta_{A(\psi)}$, where $\Delta_{A(\psi)} = \sum_j \|A_j\| \sqrt{2 \log(d_{\text{supp}(A_j)}) - 2S(\rho_j)}$, $\rho_j := \text{Tr}_{[N] \setminus \text{supp}(A_j)}(|\psi\rangle\langle\psi|)$ is the reduced density ma-

trix of $|\psi\rangle\langle\psi|$ on the subsystem of $\text{supp}(A_j)$, and $S(\rho_j)$ is the entanglement entropy of ρ_j [22]. Since $H_{\text{pert}}^\dagger H_{\text{pert}} = \sum_{j,j'} H_{\text{pert},j}^\dagger H_{\text{pert},j'}$ is a positive operator, the bound of error of the quantum dynamics is now given by the degree of entanglement entropy of various partitions, e.g., $t\|H_{\text{pert}}\|_F + \int_0^t d\tau \sqrt{\Delta_{H_{\text{pert}}^\dagger H_{\text{pert}}}(\psi(\tau))}$, where $\|X\|_F = \sqrt{\text{Tr}(X^\dagger X)/d}$, where d is the dimension of the operator X (see Supplementary Section A).

Generally, quantum states tend to be thermalized after evolution, i.e., the entropy of the subsystem grows universally. Suppose $t = c$, state entanglement is growing to case: for $t \geq c$, $\Delta_{H_{\text{pert}}}(\psi(\tau)) \approx 0$ so that $\|H_{\text{pert}}|\psi(\tau)\rangle\| \approx \|H_{\text{pert}}\|_F$. In this situation, we have

$$\|(U_0(t) - U(t))|\psi\rangle\| \lesssim \int_0^c d\tau \sqrt{\langle \psi(\tau) | H_{\text{pert}}^\dagger H_{\text{pert}} | \psi(\tau) \rangle} + (t - c)\|H_{\text{pert}}\|_F. \quad (4)$$

Here c can be efficiently estimated by measuring the expectation value of $\langle \psi(t) | H_{\text{pert}}^\dagger H_{\text{pert}} | \psi(t) \rangle$. Typically, c is a small constant; as shown in Fig. 2, we find $c \approx 0.5$ in the 1D quantum Ising model with a transverse field with specified parameters (for more numerical details, see the analog quantum simulation section). When $t \geq c$,

the error scaling exhibits average-case behavior, analogous to that for random input states, such as Haar-random states or states forming a unitary 1-design, e.g. $\int_{\psi \in \text{Harr}} d\psi \| (U_0(t) - U(t)) |\psi\rangle \| \leq t \|H_{\text{pert}}\|_F$ (see Supplementary Section A). Therefore, our entanglement-induced bound achieves the average-case scaling when $t \geq c$.

In general, the perturbation Hamiltonian H_{pert} whose error scales at most polynomially with the system size N , i.e., $\|H_{\text{pert}}\| \propto N^p$ (with $p = 1$ for linear scaling). Our results show that entanglement confers intrinsic robustness against dynamical errors, so that error bounds are expressed in the normalized Frobenius norm $\|H_{\text{pert}}\|_F$ instead of the spectral norm $\|H_{\text{pert}}\|$; this, in turn, affords tighter and more reliable analyses of quantum dynamics since $\|H_{\text{pert}}\|_F \leq \|H_{\text{pert}}\|$. For example, if H_{pert} comprises N bounded error terms, then one generally has $\|H_{\text{pert}}\| \propto N$ and $\|H_{\text{pert}}\|_F \propto \sqrt{N}$. This indicates that our entanglement-based analysis suggests a potential quadratic improvement over the worst-case scenario, as the normalized Frobenius norm typically captures average performance [46–48].

Besides, the statistical properties of disorder $\sum_k \delta_k V_k$ may also cancel some errors in quantum dynamics [49]. Suppose δ_k is a random parameter of Gaussian distribution with $\mathbb{E}\delta_k = 0$ and $\text{Var}(\delta_k) = \sigma_k^2$. By considering the nature of δ_k , the density matrix of the real evolved state is given as $\rho(t) = \mathbb{E}_{\{\delta_1, \delta_2, \dots\}} U(t) |\psi\rangle \langle \psi| U^\dagger(t)$. We find and numerically test that the upper bound of the trace distance $\|\rho_0(t) - \rho(t)\|_1$ is determined by the variance of disorder and the imperfection of coupling, which mainly contribute to the error of the evolved density matrix, where entanglement only has an inhibitory effect on the imperfection crosstalk terms (See section C in Materials and Methods).

II. ANALOG QUANTUM SIMULATION

In this section, we focus on analog quantum simulation [3, 50, 51]. Building on the general analysis of quantum dynamics presented above, we numerically demonstrate that entanglement plays a pivotal role in suppressing simulation errors. We first test the one-dimensional (1D) quantum Ising model with a transverse field (QIMF). Specifically, the Hamiltonian of 1D QIMF is given as,

$$H_0 = h_x \sum_{i=1}^N X_i + h_y \sum_{i=1}^N Y_i + J \sum_i X_i X_{i+1}, \quad (5)$$

where the parameters $h_x = 0.809, h_y = 0.9045, J = 1$ [52]. We assume that the empirical Hamiltonian is $H = H_0 + H_{\text{pert}}$. The source of perturbation H_{pert} includes stochastic disorder $H_{\text{dis}} = \sum_k \delta_k V_k$ and intrinsic imperfections $H_{\text{imp}} = \sum_m \eta_m N_m$, i.e., $H_{\text{pert}} = H_{\text{dis}} + H_{\text{imp}}$. In our numerical tests, the disorder term H_{dis} is set as a combination of N single-qubit Pauli operators X_i 's, i.e.,

$H_{\text{dis}} = \sum_{i=1}^N \delta_i X_i$, where δ_i is randomly chosen with respect to a normal distribution and X_i represents Pauli X acting on the i -th qubit. The imperfection term is set as $H_{\text{imp}} = \eta \sum_{i=1}^{N-1} X_i X_{i+1}$, where η is a constant.

We compare the simulation error for a typical initial state versus an atypical initial state. Fig. 2 (a) demonstrates the tightness of our theoretical result for long-time analog simulations. In typical scenarios ($|\psi(0)\rangle = |0\rangle^{\otimes N}$), where the entanglement entropy grows during the system's evolution, our estimate closely matches the average-case performance, scaling with $\|H_{\text{pert}}\|_F$. In contrast, in atypical cases ($|\psi(0)\rangle = |+\rangle^{\otimes N}$), where entanglement remains low, the error scaling deviates significantly and is closer to the worst-case spectral norm bound $\|H_{\text{pert}}\|$. Fig. 2 (b) further illustrates how entropy growth correlates with error suppression: rapid entropy increase corresponds to error reduction near the average estimate, while low entropy is associated with larger errors. This comparison highlights the role of entanglement in suppressing analog simulation errors, as captured by our upper bounds. Additional validation in a 2D QIMF model is provided in Supplementary Section C.

Another case study is the Fermi-Hubbard model, which is fundamental in condensed matter physics, used to describe interacting fermions on a lattice [29–32]. It captures the competition between kinetic energy and on-site Coulomb repulsion, providing insights into phenomena such as magnetism, metal-insulator transitions, and high-temperature superconductivity. We consider a 1D Fermi-Hubbard chain with periodic boundary conditions, governed by the Hamiltonian

$$H_0 = - \sum_{i=1}^L \sum_{\sigma} (a_{i,\sigma}^\dagger a_{i+1,\sigma} + \text{H.c.}) + V \sum_{i=1}^L a_{i,\uparrow}^\dagger a_{i,\uparrow} a_{i,\downarrow}^\dagger a_{i,\downarrow}, \quad (6)$$

where $\sigma = \uparrow, \downarrow$, V denotes the on-site Coulomb repulsion, $a_{i,\sigma}, a_{i,\sigma}^\dagger$ represent annihilation and creation operators, respectively. These operators are characterized by the anticommutation expressed as

$$\{a_i, a_j^\dagger\} = \delta_{ij}, \quad \{a_i, a_j\} = \{a_i^\dagger, a_j^\dagger\} = 0. \quad (7)$$

The dynamics of Fermi-Hubbard model keeps the particle number $N = \sum_i (a_{i,\uparrow}^\dagger a_{i,\uparrow} + a_{i,\downarrow}^\dagger a_{i,\downarrow})$ and the z-component of the total spin $S_z = \sum_i (a_{i,\uparrow}^\dagger a_{i,\uparrow} - a_{i,\downarrow}^\dagger a_{i,\downarrow})$ invariant, with periodic boundary condition ensures the lattice translational symmetry.

In our numerical simulations, we introduce an additional Coulomb perturbation (error term) to the Hamiltonian, i.e.,

$$H_{\text{pert}} = \delta \sum_{i=1}^L a_{i,\uparrow}^\dagger a_{i,\uparrow} a_{i,\downarrow}^\dagger a_{i,\downarrow}. \quad (8)$$

To analyze the error at each time step, we discretize the evolution into multiple short segments, each with a duration of $\Delta t = 0.1$. The one-segment simulation error is defined as $\|U(\Delta t) - U_0(\Delta t) |\psi(t)\rangle\|$. Here the initial state

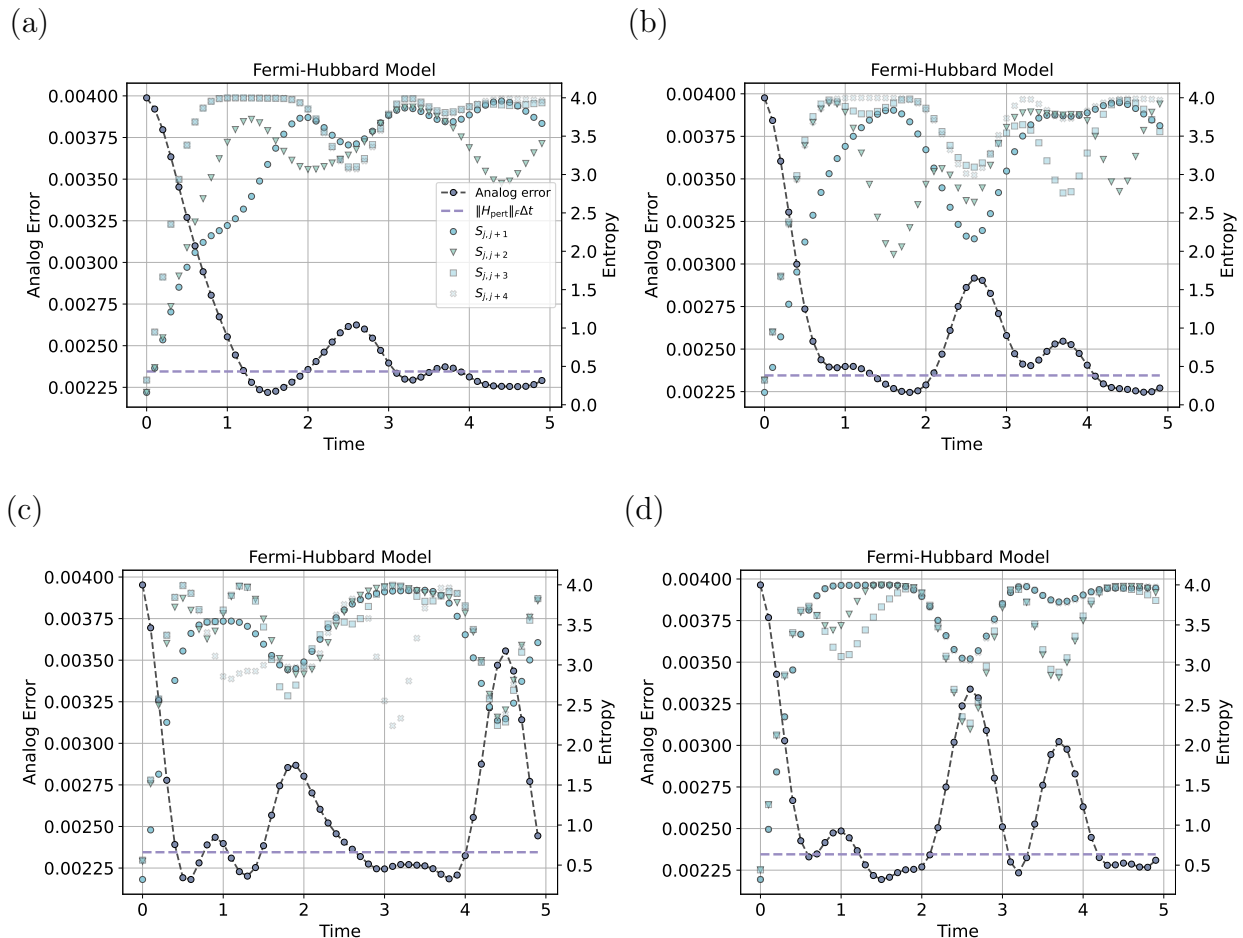


FIG. 3: Error of one-segment analog simulation with Fermi-Hubbard model. The vertical axis represents the corresponding empirical error for each individual segment with segment length $\Delta t = 0.1$. The system scale is set as $L = 8$ and the noise strength is $\delta = 0.01$. The initial state is prepared as (a) $|\uparrow\downarrow\rangle_1 |\uparrow\downarrow\rangle_2 |\uparrow\downarrow\rangle_3 |\uparrow\downarrow\rangle_4$, (b) $|\uparrow\downarrow\rangle_1 |\uparrow\downarrow\rangle_2 |\uparrow\downarrow\rangle_4 |\uparrow\downarrow\rangle_5$, (c) $|\uparrow\downarrow\rangle_1 |\uparrow\downarrow\rangle_3 |\uparrow\downarrow\rangle_5 |\uparrow\downarrow\rangle_7$, (d) $|\uparrow\downarrow\rangle_1 |\uparrow\downarrow\rangle_3 |\uparrow\downarrow\rangle_4 |\uparrow\downarrow\rangle_6$. The entanglement entropy is defined on the subsystem of two sites numbered as $(j, j + 1)$, $(j, j + 2)$, $(j, j + 3)$, $(j, j + 4)$, respectively. Entanglement entropy and the simulation error display an inverse relationship: as the entanglement entropy increases to the maximum 4 during the evolution, the simulation error reduces to the Frobenius norm level; when the entanglement entropy drops, the error exhibits sharp spikes.

is set as $\otimes_{i=1}^4 |\uparrow\downarrow\rangle_{i_1}$, which produces the maximal simulation error with noise model H_{pert} and particle number $N = 8$. The entanglement entropy is defined on subsystems with two sites (see Materials and Methods for more details). Fig. 3 depicts the relationship between one-segment simulation errors and entanglement entropy. A clear inverse correlation is observed: as entanglement entropy increases, the dynamical error decreases; conversely, as entanglement entropy decreases, the error increases. This trend highlights the inverse correlation between entanglement growth and dynamical error, which is perfectly match our theoretical analysis. We present the numerical results for the one-segment error at longer times in Fig. 7 (Materials and Methods).

III. DYNAMICAL ENTANGLEMENT DETECTION WITH ERROR SUBSPACES

Our results show that, although the error bound is formally captured by measurements of $H_{\text{pert}}^\dagger H_{\text{pert}}$, the unknown coefficients of individual noise terms make such measurements impractical. What is experimentally accessible, however, is the *structure* of the noise—the Pauli operators dictated by the device architecture.

This suggest measuring the expectations of these structure terms—akin to correlation functions—probes entanglement across specified partitions. For any traceless local Pauli operator P , the expectation $\langle \psi | P | \psi \rangle$ approaches zero when the reduced state on its support becomes nearly maximally mixed, indicating

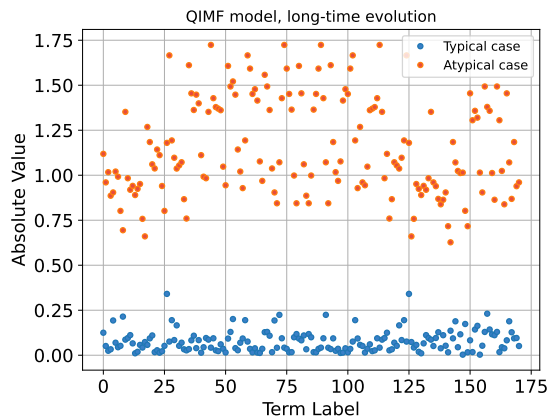


FIG. 4: The contribution of Hermitian cross terms for both the typical and the atypical cases. The noise terms include both disorder and control imperfections. The Hermitian contribution is defined as $\langle \psi(t) | H_{\text{pert},j}^\dagger H_{\text{pert},j'} + \text{H.C.} | \psi(t) \rangle / \| H_{\text{pert},j}^\dagger \| \| H_{\text{pert},j'} \|$, where $|\psi(t=6)\rangle$ is the evolved state for typical and atypical cases and $H_{\text{pert},j'}$ is a Pauli string component in the perturbation Hamiltonian. These observables track whether the error behaves close to the Frobenius norm (typical) or drifts toward spectral-norm (atypical) scaling.

strong entanglement. The operator $H_{\text{pert}}^\dagger H_{\text{pert}}$ contains cross terms $H_{\text{pert},j}^\dagger H_{\text{pert},j'} / \| H_{\text{pert},j} \| \| H_{\text{pert},j'} \|$ with coefficient-independent weights, making their expectation values experimentally accessible correlation probes.

Specifically, if for all pairs $j \neq j'$, $\langle \psi(t) | H_{\text{pert},j}^\dagger H_{\text{pert},j'} + \text{H.C.} | \psi(t) \rangle / \| H_{\text{pert},j} \| \| H_{\text{pert},j'} \| \approx 0$, the error behavior is Frobenius-norm-like, consistent with substantial entanglement within the supports $\text{supp } H_{\text{pert},j}$. By contrast, significant deviations from zero suggest limited entanglement, and the error may be close to the spectral norm case.

Figure 4 illustrates these ideas in a disordered 1D QIMF with control imperfections (the same model as in the first analog setting). For typical initial states at $t = 6$, more than 170 pairs of cross-term operators exhibit expectations near zero, indicating substantial entanglement generated during the evolution and consistent with Frobenius-norm-like error behavior. In contrast, atypical initial states yield many nonzero expectations, indicating limited entanglement growth. These results show that measuring such correlation functions provides an effective diagnostic of dynamical entanglement across the partitions of interest [53].

Note that this criterion provides a necessary—but not sufficient—condition for strong entanglement; conversely, a significant nonzero value is sufficient to rule out high entanglement (a separability witness). To reliably confirm the entanglement, we recommend measuring additional observables—at least two Pauli operators (e.g., XX and ZZ), whose joint statistics provide complementary con-

straints on the structure of the state and yield a more robust indication of genuine entanglement.

IV. QUANTUM CONTROL PROTOCOLS

Another important application of our analysis lies in quantum control—the design and implementation of protocols that manipulate quantum systems to realize quantum gates with high fidelity.

We consider implementing a k -qubit gate on an n -qubit register. In general, the k target qubits are coupled to m neighboring spectator qubits (often referred to as spectators or intruders [54]); together, these $k + m$ qubits form a subsystem of the full n -qubit system. We denote by $H^{m,k}(t)$ the Hamiltonian with quantum control acting on the $m + k$ -qubit (targets + neighbors), and its evolution is $U(t)$. The ideal gate $U_0(t)$ is generated by the ideal Hamiltonian $H_{\text{ideal}}(t)$ on the target subspace.

For an initial n -qubit state $|\psi\rangle$, the effective error of the quantum gate can be given as $\| (I_{n \setminus k} \otimes U_0(t) - I_{n \setminus (m+k)} \otimes U(t)) |\psi\rangle \|$, which we hereafter simplify to $\| (U_0(t) - U(t)) |\psi\rangle \|$ by omitting the identity operators. To illustrate the effects of entanglement in quantum control in a simple and clear manner, we partition the entire system into two subsystems, A and B . Let A denote the system of $m + k$ qubits, and B denote the system of the remaining qubits $n - m - k$, and now $|\psi\rangle = |\psi\rangle_{AB}$ (as shown in Fig. 5 (a)). By utilizing our entanglement-based result of time-dependent analysis (see Materials and Methods), one may have $\| (U_0(t)_A - U(t)_A) |\psi\rangle_{AB} \| \approx \int_0^t d\tau \| (H_{\text{ideal}}(\tau) - H^{m,k}(\tau)) \|_F$ for large entangled state $|\psi\rangle_{AB}$. This suggests that entanglement can induce robustness in implementing quantum gates with quantum control protocols.

To demonstrate how entanglement enhances quantum control of quantum gates, we perform numerical simulations of quantum gate implementation on a 3×4 qubit 2D quantum dot system (see the lattice in Fig. 5 (c)). Specifically, to realize the Pauli gate $U(\theta) = \exp(-iX_t\theta)$ on the target k qubit (here $k = 1$, and the target qubit is surrounded by orange circle in Fig. 5 (c)), one drives the system with an ideal control field that generates the single-qubit Hamiltonian $H_{\text{ideal}} = \frac{\Omega(t)}{2} X_k$. Nevertheless, imperfections in the inter-qubit couplings, together with (random) drift of the control and frequency, generate a total time-dependent perturbation term $H_{\text{pert}}(t) = H_{\text{drift}} + H^{m,k} - H_{\text{ideal}}$ in the Hamiltonian. The perturbation Hamiltonian is then expressed accordingly (see

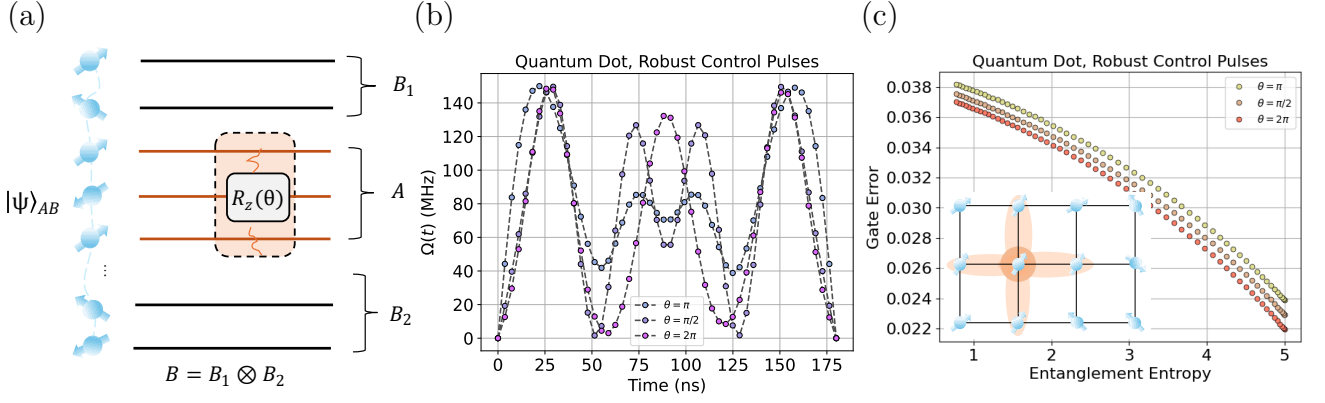


FIG. 5: Subsystem entanglement and gate error. (a) Schematic partition of a quantum-control circuit for a target single-qubit gate into subsystem A (the target qubit plus nearby qubits directly coupled to the control fields) and subsystem B (the remaining register qubits). (b) Quantum-dot system driven with robust control pulses for a single-qubit gate. The optimal driving waveform for implement time $T = 180\text{ns}$ and target gates X_π , $X_{\pi/2}$, $X_{2\pi}$, respectively. (c) Dependence of effective gate error on the entanglement entropy (higher temperature of purified Gibbs state, higher entanglement entropy) of the initial states with corresponding waveforms. We consider a 2D lattice in which 4 spectator qubits couple to the target (so $|A| = 5$ and $S_{\max} = \log(2^5) = 5$). States are sampled as Gibbs states with temperatures T chosen as $T \in \{\frac{1}{t} | t \in \{0.008, 0.016, \dots, 0.48\}\}$ (equivalently T spanning ≈ 2.08 to 125). As the entanglement entropy $S(A)$ approaches its maximum, the error bound rapidly decreases, indicating that greater preexisting entanglement between A and B suppresses the influence of gate imperfections.

Supplementary section B)

$$\begin{aligned}
 H_{\text{pert}}(t) &= \delta \sum_{i \in R_k} Z_i + \epsilon \Omega_k(t) X_k \\
 &+ \frac{J}{4} \sum_{i \in R_k} Z_i Z_k + \frac{\tan \theta \Omega_k(t)}{2} \\
 &\times \sum_{i \in R_k} \left[\cos(\Delta \tilde{E}_z t) X_i Z_k - \sin(\Delta \tilde{E}_z t) Y_i Z_k \right],
 \end{aligned} \tag{9}$$

where R_k represents the target qubit and its adjacent qubits as illustrated by orange ovals in Fig. 5 (c) where $k = 1$ and $m = 4$ ($|R_k| = 4$). For best control accuracy, we can set the driving field $\Omega(t)$ as a robust control pulse (RCP) [55]. We test the performance of RCPs for 3 different target gates X_π , $X_{\pi/2}$, $X_{2\pi}$. The gate time is $T = 180\text{ns}$, and the waveform of these RCPs are demonstrated in Fig. 5 (b).

To show the relationship between entanglement entropy and the faithfulness of the implementation of quantum gates, we consider a set of two-partite purified Gibbs states or thermofield double states [56],

$$|\psi_T\rangle_{AB} = \frac{\sum_i e^{-\epsilon_i/T} |\phi_i\rangle_{R_k} |\phi_i^*\rangle_{B_1}}{\|\sum_i e^{-\epsilon_i/T} |\phi_i\rangle_{R_k} |\phi_i^*\rangle_{B_1}\|} \otimes |0\rangle_{B_2}^{\otimes 2}, \tag{10}$$

where the system is divided into R_k and the complementary part. B_1 consists of 5 qubits responding to R_k , while B_2 represents the other 2 qubits. Here $\{(\epsilon_i, \phi_i)\}$'s are eigenvalues and eigenvectors of the 5-qubit Hamiltonian $V = -\sum_{i \in R_k} Z_i$. The entanglement entropy of

$|\psi_T\rangle$ increases as the temperature T increases. Fig. 5(c) shows the relationship between the entanglement entropy and the gate error, with parameters $\Delta E_Z = 200\text{MHz}$, $J = 100\text{kHz}$, $\delta = 50\text{kHz}$, $\epsilon = 0.001$ and $\theta = \arctan \frac{J}{2\Delta E}$. The error quickly reduces when the entanglement rises close to its maximum. This suggests that higher entanglement is correlated with improved fidelity, indicating that entanglement can further enhance the robustness of quantum control protocols even with RCPs already applied. Additional validation of a class of two-qubit gates in a 2D quantum dot system is provided in Supplementary Section C.

V. DISCUSSIONS AND CONCLUSIONS

Our results demonstrate that the dynamical growth of many-body entanglement can provide intrinsic protection against the coherent and perturbative noises of quantum dynamics. In the context of the Eigenstate Thermalization Hypothesis [57, 58], this implies a fundamental connection between error proliferation and the entanglement and thermalization of the system—a connection that persists even in regimes of incomplete thermalization. Moreover, extending these ideas to non-Hermitian quantum dynamics (Parity-Time symmetry system [59, 60]) indicates that entanglement may still serve as a vital resource in mitigating errors. Recent studies have shown that entanglement can even protect against noise in cross-platform protected qubits [61] and

operator dynamic simulation [23], suggesting that harnessing entanglement could be a powerful strategy in developing noise-resilient quantum technologies.

Translating these insights into the language of quantum circuits, we define the error unitary as the product of the ideal circuit U_0 and the approximate circuit U (see section D in Supplementary Materials). Our entanglement-based analysis of quantum circuits suggest that, given a fixed initial state, entanglement growth in a quantum circuit decreases the sensitivity of parameter changes in the sequential circuit so which may induce phenomena such as barren plateaus [62, 63], hindering the efficiency of variational algorithms. While rapid entanglement generation can impede gradient-based optimization, from a state preparation perspective [64, 65], it enhances robustness against noise. This dual role underscores the importance of balancing entanglement control: suppressing excessive growth to facilitate optimization, while leveraging its benefits to improve system stability.

In general, harnessing entanglement provides a quantitative framework for understanding and enhancing the stability of complex quantum systems, thereby facilitating the development of noise-resilient quantum technologies. On a fundamental level, these insights may connect to phenomena such as quantum phase transitions [66–68] and the emergence of robust properties or classical behavior from quantum many-body systems [69]. Understanding these connections deepens our comprehension of the fundamental physics and could inspire new strategies for designing robust quantum devices capable of operating in noisy environments.

MATERIALS AND METHODS

A. Universal error Upper bound for time-dependent Hamiltonian

The derivation of our main results will be based on the following lemma concerning a time-dependent Hamiltonian.

Lemma 1. [44] *Let $A(t)$ and $B(t)$ be continuous time-dependent Hermitian operators, and let $U_A(t)$ and $U_B(t)$ with $U_A(0) = U_B(0) = I$ be the corresponding time evolution unitaries. Then $W(t) = U_B(t)^\dagger U_A(t)$ is the unique solution of $i\partial_t W(t) = U_B(t)^\dagger (A(t) - B(t)) U_B(t) W(t)$, and $W(0) = I$.*

Suppose $A(t) = H_0(t)$ is the ideal Hamiltonian and $B(t) = H'(t)$ which is the noise Hamiltonian, we have $W(t) = U_B(t)^\dagger U_A(t) = \mathcal{T} e^{\int_{s_1=0}^t ds_1 iH'(s_1)} \mathcal{T} e^{-\int_{s_2=0}^t ds_2 iH_0(s_2)}$. Define $\mathcal{D} = \|(U_A(t) - U_B(t))|\psi\rangle\|$. By making use of Lemma 2, we bound the dynamical error as

$$\begin{aligned}
\mathcal{D} &= \|U_B(t)(W(t) - I)|\psi\rangle\| \\
&= \|(W(t) - I)|\psi\rangle\| \\
&= \|(W(t) - W(0))|\psi\rangle\| \\
&= \left\| i \int_0^t dt \partial_t W(t) |\psi\rangle \right\| \\
&= \left\| \left[\int_0^t d\tau U_B(\tau)^\dagger (A(\tau) - B(\tau)) U_B(\tau) W(\tau) \right] |\psi\rangle \right\| \\
&= \left\| \left[\int_0^t d\tau U_B(\tau)^\dagger (A(\tau) - B(\tau)) U_A(\tau) \right] |\psi\rangle \right\| \\
&\leq \int_0^t d\tau \|(A(\tau) - B(\tau)) U_A(\tau) |\psi\rangle\| \\
&= \int_0^t d\tau \|[H'(\tau) - H_0(\tau)] e^{-\int_s^\tau ds iH(s)} |\psi\rangle\| \\
&= \int_0^t d\tau \|[H'(\tau) - H_0(\tau)] |\psi(\tau)\rangle\|.
\end{aligned} \tag{11}$$

In the derivation above, we have used the norm-preserving property of the unitary operator: $\|UX|\psi\rangle\| = \|X|\psi\rangle\|$ for any operator X . Our result suggest, for a time-dependent Hamiltonian, the upper bound of error term in the state vector reduces to $H'(\tau) - H_0(\tau)$, where $|\psi(\tau)\rangle$ denotes the ideal time-evolved state at evolution time τ .

B. Entanglement-based bound of time-dependent Hamiltonian

In general, the perturbative Hamiltonian, $H_{\text{pert}} = H'(\tau) - H_0(\tau)$, may be time-dependent, e.g, $H_{\text{pert}}(\tau)$. To investigate the role of entanglement in bounding the error for such time-dependent cases, we discretize the total evolution time t into J segments of duration $\Delta t = t/J$. The upper bound $\int_0^t d\tau \|H_{\text{pert}}(\tau) |\psi(\tau)\rangle\|$ can then be rewritten as a sum over these segments:

$$\sum_{j=0}^{J-1} \int_{j\Delta t}^{(j+1)\Delta t} d\tau \sqrt{\langle \psi(\tau) | H_{\text{pert}}^\dagger(\tau) H_{\text{pert}}(\tau) | \psi(\tau) \rangle}. \tag{12}$$

A key mathematical relationship is employed. For an operator $A = \sum_j A_j$ composed of non-trivial local operators A_j , the following inequality holds [22]

$$\langle \psi | A^\dagger A | \psi \rangle \leq \|A\|_F^2 + \Delta_{A^\dagger A}(\psi), \tag{13}$$

where $\Delta_{A^\dagger A}(\psi) = \sum_j \|A_j\| \sqrt{2 \log(d_{\text{supp}(A_j)} - 2S(\rho_j))}$, $\|\cdot\|_F$ denotes the normalized Frobenius norm, $\rho_j := \text{Tr}_{[N] \setminus \text{supp}(A_j)}(|\psi\rangle\langle\psi|)$ is the reduced density matrix of $|\psi\rangle\langle\psi|$ on the subsystem of $\text{supp}(A_j)$, and $S(\rho_j)$ is the entanglement entropy of ρ_j . Defining $A_{j\Delta t}^{(j+1)\Delta t} = \int_{j\Delta t}^{(j+1)\Delta t} d\tau H_{\text{pert}}^\dagger(\tau) H_{\text{pert}}(\tau)$ as a positive operator for

segment j , we bound the dynamical error as (see Supplementary Section A for details)

$$\begin{aligned} \|(U_A(t) - U_B(t))|\psi(0)\rangle\| &\leq (\Delta t)^{\frac{1}{2}} \sum_{j=0}^{J-1} \sqrt{\frac{\text{Tr}(A_{j\Delta t}^{(j+1)\Delta t})}{d}} \\ &+ \sum_{j=0}^{J-1} \int_{j\Delta t}^{(j+1)\Delta t} d\tau \sqrt{\Delta H_{\text{pert}}^\dagger(\tau) H_{\text{pert}}(\tau)}(\psi(\tau)). \end{aligned} \quad (14)$$

Assuming the state $|\psi(\tau)\rangle$ remains sufficiently entangled at all times, the upper bound approximately simplifies to

$$\sum_{j=0}^{J-1} (\Delta t)^{\frac{1}{2}} \sqrt{\frac{\text{Tr}(A_{j\Delta t}^{(j+1)\Delta t})}{d}} = \int_0^t \|H_{\text{pert}}(\tau)\|_F. \quad (15)$$

Finally, it can be verified that in the time-independent limit where $H_{\text{pert}}(\tau) = H_{\text{pert}}$, we have $A_{j\Delta t}^{(j+1)\Delta t} = \Delta t H_{\text{pert}}^\dagger H_{\text{pert}}$. In this case, the general upper bound in (14) reduces to

$$t \|H_{\text{pert}}\|_F + \int_0^t d\tau \sqrt{\Delta H_{\text{pert}}^\dagger(\tau) H_{\text{pert}}(\tau)}(\psi(\tau)), \quad (16)$$

which recovers the exact upper bound for the long-time error in the time-independent case in the main text.

C. Error analysis with random disorder

Suppose that $H_{\text{pert}} = V + N = \sum_k \delta_k V_k + \sum_m \eta_m N_m$ and suppose δ_k is a random parameter of Gaussian distribution with $\mathbb{E}\delta_k = 0$ and $\text{Var}(\delta_k) = \sigma_k^2$. The upper bounds of Eq. (3) and Eq. (4) are for a single run with fixed δ_k . Considering the random nature of δ_k , the density matrix of the real evolved state is given as $\rho(t) = \mathbb{E}_{\{\delta_1, \delta_2, \dots\}} U(t) |\psi\rangle \langle \psi| U^\dagger(t)$, where $U(t) = \hat{T} e^{-i \int H'(\tau) d\tau}$. Now, the distance between the ideal evolution and the approximated one should be defined by the 1-norm $\|\rho_0(t) - \rho(t)\|_1$ ($\|A\|_1 = \text{Tr}(\sqrt{A^\dagger A})$) with $\rho_0(t) = U_0(t) |\psi\rangle \langle \psi| U_0^\dagger(t)$. Since for any two projectors $|\chi\rangle \langle \chi|$ and $|\phi\rangle \langle \phi|$, the following inequality holds, e.g., $\| |\chi\rangle \langle \chi| - |\phi\rangle \langle \phi| \|_1 \leq 2\| |\psi\rangle - |\phi\rangle \|$ [70]. Now we have (see Supplementary Section A)

$$\begin{aligned} \|\rho_0(t) - \rho(t)\|_1 &\leq 2 \int_0^t d\tau \sqrt{\sum_k \sigma_k^2 + \|N|\psi(\tau)\rangle\|^2}, \\ &\leq 2t \sqrt{\sum_k \sigma_k^2} + 2 \int_0^t d\tau \|N|\psi(\tau)\rangle\|, \end{aligned} \quad (17)$$

where $N = \sum_m \eta_m N_m$. This suggests that the variance of disorder and the imperfection of coupling mainly contribute to the error of the evolved density matrix, where

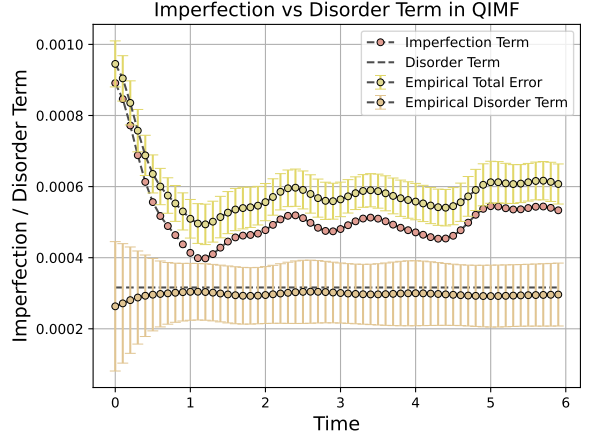


FIG. 6: Comparison between the contribution to analog simulation error of disorder and imperfection terms. Here we use the same model as that used in Figure 2. We take 30 trials for each moment, with disorder strength δ_k randomly drawn with respect to the normal distribution $\mathcal{N}(0, 0.01)$. The error bar in the figure shows the standard deviation for the 30 trials. The contribution of disorder and imperfections is defined as $\int_t^{t+\Delta t} d\tau \|V|\psi(\tau)\rangle\|$ and $\int_t^{t+\Delta t} d\tau \|N|\psi(\tau)\rangle\|$, respectively, where Δt represents the segment length. The result shows that while the average disorder contribution is almost independent of the state, the contribution of imperfections quickly converges to the entangled case as the evolution time increases.

entanglement only has an inhibitory effect on the imperfection term N . Note that the average case error $\mathbb{E}_{\{\delta_1, \delta_2, \dots\}} \|(U_0(t) - U(t))|\psi\rangle\| = \frac{1}{2} \|\rho_0(t) - \rho(t)\|_1$, while $\|\rho_0(t) - \rho(t)\|_1$ provide the rigorous upper bound of the error.

Figure 6 compares the contribution of imperfection terms and disorder terms on the analog simulation error. It shows that the average contribution of disorder terms remains at almost the same level as the system evolves, while the imperfection terms depends more on the state, which is consistent with our theoretical results.

Remarkably, if the Gaussian distribution of disorder is unbiased, i.e. $\mathbb{E}\delta_k \neq 0$, there are some cross terms consisting of the disorder terms and the imperfection terms. The error is also relate to the disorder term but entanglement can also contributes to suppress these error.

D. Fermionic lattices

In fermionic systems, the concept of entanglement fundamentally differs from that in systems of distinguishable spins. Since electrons are identical fermions obeying antisymmetric exchange statistics, the reduced density matrix for a subset of sites cannot be straightforwardly defined by tracing over individual particles. Instead, the

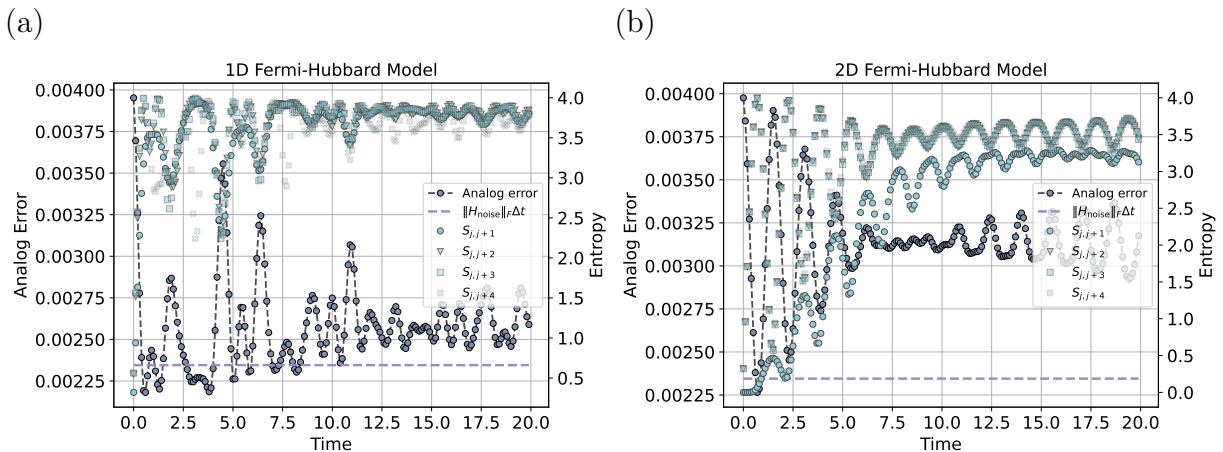


FIG. 7: Error of one-segment analog simulation with (a) 1D Fermi-Hubbard model with 8 sites and (b) 2×4 2D Fermi-Hubbard model in a longer evolution process. The Coulomb interaction strength is $U = 0.5$, the segment length is set as $\Delta t = 0.1$, and the noise strength is $\delta = 0.01$. Periodic boundary conditions are applied for both models. The initial state is prepared as $|\uparrow\downarrow\rangle_1 |\uparrow\downarrow\rangle_3 |\uparrow\downarrow\rangle_5 |\uparrow\downarrow\rangle_7$, that is, for the one-dimensional model, every second site is doubly occupied; for the two-dimensional model, each row has two doubly occupied sites. The entanglement entropy is defined on the subsystem of two sites numbered as $(j, j+1)$, $(j, j+2)$, $(j, j+3)$, $(j, j+4)$, respectively. In the long-time scale, simulation error in both 1D and 2D cases keeps oscillating. In the 1D case where the entanglement gets close to the maximum $\log 4^2 = 4$, the error oscillates around the Frobenius norm estimate. Whereas in the 2D case, where the entanglement does not increase to the maximum, a gap between the empirical error and the Frobenius norm can be observed.

entanglement is characterized by the correlations among multiple sites, each hosting a spin- $\frac{1}{2}$ fermion.

Consider a lattice Λ , with each site i hosting a fermionic mode with spin degrees of freedom described by annihilation operators $c_{i,\sigma}$, where $\sigma = \uparrow, \downarrow$. The global state ρ is represented jointly in the fermionic Fock space and the local internal Hilbert space at each site, respecting the Pauli exclusion principle. To analyze entanglement, one partitions the lattice into a subsystem $A \subseteq \Lambda$ and its complement $B = \Lambda \setminus A$. The reduced density matrix ρ_A is obtained via a fermionic partial trace $\rho_A = \text{Tr}_B(\rho)$.

Since electrons carry spin, the reduced density matrix for the region A encapsulates correlations over both spatial sites and spin degrees of freedom. The maximal entanglement entropy of a local site ($|A| = 1$) should be $S_A = -\text{Tr}(\rho_A \log \rho_A) = 2$. This emphasizes that, unlike traditional spin models where the local Hilbert space is simply two-dimensional, in fermionic systems with $1/2$ spin, the local Hilbert space of each site is 4-dimensional, behaving like 2 qubits.

Based on this fact, the analysis in the main text regarding entanglement-induced resilience is equally applicable to fermionic systems. In this context, entanglement is directly defined by the partitioning of sites; increasing entanglement among different sites enhances the overall robustness of the system's dynamics. Importantly, our focus here is on the dynamical evolution rather than on the ground state problem of the Hamiltonian, which dis-

tinguishes this work from [68].

We demonstrate additional numerical results of Fermi-Hubbard model under the perturbative noise (see Eq. (8)) with a longer time scale in Figure 7. Because of the Coulomb interaction and the Pauli exclusion principle, the Fermi-Hubbard model does not fully thermalize; as a result, the simulation error continues to oscillate. This effect is more pronounced in the 2D Fermi-Hubbard model, where the analog simulation error is obviously larger than the Frobenius norm estimate, as shown in Figure 7.

E. Quantum control

Consider implementing a k -qubit quantum gate, where the k target qubits are coupled to neighboring spectator or intruder qubits. In the physical basis, the total Hamiltonian can be expressed as $\tilde{H}^{m,k} = \tilde{H}_0 + \tilde{V}(t)$, where H_0 is the native Hamiltonian and $\tilde{V}(t)$ is the control field. To analyze coupling effects, we transform to the eigenbasis of the eigenbasis of \tilde{H}_0 , where the Hamiltonian can be decomposed into a direct sum of blocks [55]

$$H^{m,k} = \bigoplus_{i=1}^{2^m} H_i + \bigoplus_{i,j=1}^{2^m} V_{ij}(t). \quad (18)$$

The full matrix of the Hamiltonian is defined in the Supplementary Section B. Here, the superscript $m; d$ denotes

a system with m neighboring qubits affecting k target qubits. The Hamiltonian decomposes into $2^m \times 2^m$ blocks corresponding to different configurations of the neighboring qubits. For example, in a system with two neighboring qubits and one target qubit, $\text{span}\{|\uparrow\uparrow; \uparrow\rangle, |\uparrow\uparrow; \downarrow\rangle\}$ represents the $i = 1$ diagonal subspace where both neighboring qubits are in the $|\uparrow\rangle$ state.

Without loss of generality, we designate the $i = 1$ subspace as our reference and define the reference Hamiltonian $\tilde{H}_{\text{ref}} = \tilde{H}_1 + \tilde{V}_{11}$ (here the reference Hamiltonian can be set to the ideal Hamiltonian of implementation of the target quantum gate, i.e., $H_{\text{ref}} = H_{\text{ideal}}$ and $\tilde{H}_{\text{ref}} = \tilde{H}_{\text{ideal}}$). The difference between the reference and the original Hamiltonian is identified as a correlated error Hamiltonian involved with quantum control, which can be seen as one part of the perturbation Hamiltonian:

$$H_{\text{error}} = H^{m;k} - H_{\text{ref}} = \bigoplus_{i=2}^{2^m} (\Delta H_i + \Delta V_{ii}) + \bigoplus_{i,j=1, i \neq j}^{2^m} V_{ij}. \quad (19)$$

Here, $\Delta H_i = H_i - H_1$ represents frequency shifts experienced by target qubits due to different configurations of neighboring qubits, collectively forming a manifold of 2^m distinct energy levels. The terms $\Delta V_{ii} = V_{ii} - V_{11}$ represent variations in control field effects across different neighboring-qubit configurations, while $V_{ij}(t)$ for $i \neq j$ captures crosstalk between different subspaces.

Let A denote the subsystem consisting of the $m + k$ qubits (target and spectators), and B the remaining $n - m - k$ qubits, with the total state denoted as $|\psi(\tau)\rangle_{AB}$. The initial state before implementing the quantum gate is $|\psi(0)\rangle_{AB}$. Since the error Hamiltonian $H_{\text{error}}(\tau)$ in quantum control is generally time-dependent and acts locally on subsystem A , we now bound the resulting error $\|(U_0(t) - U(t))|\psi(0)\rangle_{AB}\|$ as follows (see Supplementary Section B for details):

$$\int_0^t d\tau \|H_{\text{error}}(\tau)\|_F + \int_0^t d\tau \sqrt{\|H_{\text{error}}^\dagger(\tau)H_{\text{error}}(\tau)\| \sqrt{2(\log d_A - S(\rho_A(\tau)))}}. \quad (20)$$

When the entanglement in $|\psi(\tau)\rangle_{AB}$ is sufficiently large during the control period, the error is dominated by the normalized Frobenius norm of the error Hamiltonian, yielding the approximation $\|(U_0(t) - U(t))|\psi(0)\rangle\| \approx \int_0^t d\tau \|H_{\text{error}}(\tau)\|_F$.

It is noteworthy that entanglement within subsystem A (between targets and spectators) also aids in noise suppression. For a clear presentation, here we treat all components inside A as a unified subsystem, instead of separating them into multiple subspaces corresponding to different $H_{\text{error}}^{(j)}(\tau)$.

Acknowledgment: Q.Z. acknowledges funding from Innovation Program for Quantum Science and Technology via Project 2024ZD0301900, National Natural Science Foundation of China (NSFC) via Project No. 12347104 and No. 12305030, Guangdong Basic and Applied Basic Research Foundation via Project 2023A1515012185, Hong Kong Research Grant Council (RGC) via No. 27300823, N_HKU718/23, and R6010-23, Guangdong Provincial Quantum Science Strategic Initiative No. GDZX2303007, HKU Seed Fund for Basic Research for New Staff via Project 2201100596. X. L. thanks the National Basic Research Program of China (Grants No. 2021YFA1400900). X.-H.D. thanks the Shenzhen Science and Technology Program (KQTD20200820113010023) and the Innovation Program for Quantum Science and Technology (2024ZD0300400). **Code availability:** The code used in this study is available via GitHub: <https://github.com/minidas/analog>.

-
- [1] I. M. Georgescu, S. Ashhab, and F. Nori, Quantum simulation, *Rev. Mod. Phys.* **86**, 153 (2014).
 - [2] J. Preskill, Quantum computing and the entanglement frontier (2012), arXiv:1203.5813 [quant-ph].
 - [3] I. Buluta and F. Nori, Quantum simulators, *Science* **326**, 108 (2009).
 - [4] D. Gottesman, Theory of fault-tolerant quantum computation, *Phys. Rev. A* **57**, 127 (1998).
 - [5] D. A. Abanin, E. Altman, I. Bloch, and M. Serbyn, Colloquium: Many-body localization, thermalization, and entanglement, *Rev. Mod. Phys.* **91**, 021001 (2019).
 - [6] P. W. Anderson, Absence of diffusion in certain random lattices, *Phys. Rev.* **109**, 1492 (1958).
 - [7] M. Heyl, Dynamical quantum phase transitions: a review, *Reports on Progress in Physics* **81**, 054001 (2018).
 - [8] L. Wang, Y.-H. Liu, J. Imriška, P. N. Ma, and M. Troyer, Fidelity susceptibility made simple: A unified quantum monte carlo approach, *Physical Review X* **5**, 031007 (2015).
 - [9] P. Zhao, K. Linghu, Z. Li, P. Xu, R. Wang, G. Xue, Y. Jin, and H. Yu, Quantum crosstalk analysis for simultaneous gate operations on superconducting qubits, *PRX Quantum* **3**, 020301 (2022).
 - [10] P. Doria, T. Calarco, and S. Montangero, Optimal control technique for many-body quantum dynamics, *Physical review letters* **106**, 190501 (2011).
 - [11] C. Altafini and F. Ticozzi, Modeling and control of quantum systems: An introduction, *IEEE Transactions on Automatic Control* **57**, 1898 (2012).
 - [12] I. Schwenk, S. Zanker, J.-M. Reiner, J. Leppäkangas, and M. Marthaler, Estimating the error of an analog quantum simulator by additional measurements, *Physical Review*

- Letters **119**, 240502 (2017).
- [13] K. Fukui, A. Tomita, A. Okamoto, and K. Fujii, High-threshold fault-tolerant quantum computation with analog quantum error correction, *Physical review X* **8**, 021054 (2018).
- [14] L. Viola, E. Knill, and S. Lloyd, Dynamical decoupling of open quantum systems, *Phys. Rev. Lett.* **82**, 2417 (1999).
- [15] H. Bombín, Resilience to time-correlated noise in quantum computation, *Phys. Rev. X* **6**, 041034 (2016).
- [16] L. Amico, R. Fazio, A. Osterloh, and V. Vedral, Entanglement in many-body systems, *Rev. Mod. Phys.* **80**, 517 (2008).
- [17] R. Horodecki, P. Horodecki, M. Horodecki, and K. Horodecki, Quantum entanglement, *Rev. Mod. Phys.* **81**, 865 (2009).
- [18] J. Eisert, M. Cramer, and M. B. Plenio, Colloquium: Area laws for the entanglement entropy, *Rev. Mod. Phys.* **82**, 277 (2010).
- [19] C. H. Bennett, G. Brassard, C. Crépeau, R. Jozsa, A. Peres, and W. K. Wootters, Teleporting an unknown quantum state via dual classical and einstein-podolsky-rosen channels, *Physical review letters* **70**, 1895 (1993).
- [20] R. Jozsa, Entanglement and quantum computation, *arXiv preprint quant-ph/9707034* (1997).
- [21] V. Giovannetti, S. Lloyd, and L. Maccone, Advances in quantum metrology, *Nature photonics* **5**, 222 (2011).
- [22] Q. Zhao, Y. Zhou, and A. M. Childs, Entanglement accelerates quantum simulation, *Nature Physics* **21**, 1338–1345 (2025).
- [23] T. Feng, Y. Cao, and Q. Zhao, Trotterization, operator scrambling, and entanglement (2025), *arXiv:2506.23345 [quant-ph]*.
- [24] S. Lloyd, Universal Quantum Simulators, *Science* **273**, 1073 (1996).
- [25] A. M. Childs, Y. Su, M. C. Tran, N. Wiebe, and S. Zhu, Theory of Trotter Error with Commutator Scaling, *Phys. Rev. X* **11**, 011020 (2021), *arXiv:1912.08854*.
- [26] G. H. Low and I. L. Chuang, Hamiltonian Simulation by Qubitization, *Quantum* **3**, 163 (2019), *arXiv:1610.06546*.
- [27] D. W. Berry, A. M. Childs, R. Cleve, R. Kothari, and R. D. Somma, Simulating Hamiltonian dynamics with a truncated Taylor series, *Phys. Rev. Lett.* **114**, 090502 (2015), *arXiv:1412.4687*.
- [28] A. M. Childs, D. Maslov, Y. Nam, N. J. Ross, and Y. Su, Toward the first quantum simulation with quantum speedup, *Proc Natl Acad Sci USA* **115**, 9456 (2018).
- [29] D. P. Arovas, E. Berg, S. A. Kivelson, and S. Raghu, The hubbard model, *Annual review of condensed matter physics* **13**, 239 (2022).
- [30] T. Esslinger, Fermi-hubbard physics with atoms in an optical lattice, *Annu. Rev. Condens. Matter Phys.* **1**, 129 (2010).
- [31] R. A. Hart, P. M. Duarte, T.-L. Yang, X. Liu, T. Paiva, E. Khatami, R. T. Scalettar, N. Trivedi, D. A. Huse, and R. G. Hulet, Observation of antiferromagnetic correlations in the hubbard model with ultracold atoms, *Nature* **519**, 211 (2015).
- [32] H.-J. Shao, Y.-X. Wang, D.-Z. Zhu, Y.-S. Zhu, H.-N. Sun, S.-Y. Chen, C. Zhang, Z.-J. Fan, Y. Deng, X.-C. Yao, *et al.*, Antiferromagnetic phase transition in a 3d fermionic hubbard model, *Nature* **632**, 267 (2024).
- [33] H. Bernien, S. Schwartz, A. Keesling, H. Levine, A. Omran, H. Pichler, S. Choi, A. S. Zibrov, M. Endres, M. Greiner, *et al.*, Probing many-body dynamics on a 51-atom quantum simulator, *Nature* **551**, 579 (2017).
- [34] J. Simon, W. S. Bakr, R. Ma, M. E. Tai, P. M. Preiss, and M. Greiner, Quantum simulation of antiferromagnetic spin chains in an optical lattice, *Nature* **472**, 307 (2011).
- [35] C. Gross and I. Bloch, Quantum simulations with ultracold atoms in optical lattices, *Science* **357**, 995 (2017).
- [36] B. Yang, H. Sun, R. Ott, H.-Y. Wang, T. V. Zache, J. C. Halimeh, Z.-S. Yuan, P. Hauke, and J.-W. Pan, Observation of gauge invariance in a 71-site bose-hubbard quantum simulator, *Nature* **587**, 392 (2020).
- [37] U.-J. Wiese, Ultracold quantum gases and lattice systems: quantum simulation of lattice gauge theories, *Annalen der Physik* **525**, 777 (2013).
- [38] S. P. Jordan, K. S. Lee, and J. Preskill, Quantum algorithms for quantum field theories, *Science* **336**, 1130 (2012).
- [39] Z.-Y. Zhou, G.-X. Su, J. C. Halimeh, R. Ott, H. Sun, P. Hauke, B. Yang, Z.-S. Yuan, J. Berges, and J.-W. Pan, Thermalization dynamics of a gauge theory on a quantum simulator, *Science* **377**, 311 (2022).
- [40] J. I. Cirac, D. Perez-Garcia, N. Schuch, and F. Verstraete, Matrix product states and projected entangled pair states: Concepts, symmetries, theorems, *Reviews of Modern Physics* **93**, 045003 (2021).
- [41] R. Orús, Tensor networks for complex quantum systems, *Nature Reviews Physics* **1**, 538 (2019).
- [42] M. McEwen, D. Kafri, Z. Chen, J. Atalaya, K. Satzinger, C. Quintana, P. V. Klimov, D. Sank, C. Gidney, A. Fowler, *et al.*, Removing leakage-induced correlated errors in superconducting quantum error correction, *Nature communications* **12**, 1761 (2021).
- [43] P. M. Harrington, M. Li, M. Hays, W. Van De Pontseele, D. Mayer, H. D. Pinckney, F. Contipelli, M. Gingras, B. M. Niedzielski, H. Stickler, *et al.*, Synchronous detection of cosmic rays and correlated errors in superconducting qubit arrays, *Nature Communications* **16**, 6428 (2025).
- [44] J. Haah, M. Hastings, R. Kothari, and G. H. Low, Quantum algorithm for simulating real time evolution of lattice hamiltonians, in *2018 IEEE 59th Annual Symposium on Foundations of Computer Science (FOCS)* (2018) pp. 350–360.
- [45] M. A. Nielsen, M. R. Dowling, M. Gu, and A. C. Doherty, Quantum computation as geometry, *Science* **311**, 1133 (2006), <https://www.science.org/doi/pdf/10.1126/science.1121541>.
- [46] Q. Zhao, Y. Zhou, A. F. Shaw, T. Li, and A. M. Childs, Hamiltonian simulation with random inputs, *Phys. Rev. Lett.* **127**, 270502 (2021), *arXiv:2111.04773*.
- [47] C.-F. Chen and F. G. Brandão, Average-case speedup for product formulas, *Communications in Mathematical Physics* **405**, 32 (2024).
- [48] G. D. Kahanamoku-Meyer, J. Blue, T. Bergamaschi, C. Gidney, and I. L. Chuang, A log-depth in-place quantum fourier transform that rarely needs ancillas (2025), *arXiv:2505.00701 [quant-ph]*.
- [49] Y. Cai, Y. Tong, and J. Preskill, Stochastic error cancellation in analog quantum simulation (Schloss Dagstuhl – Leibniz-Zentrum für Informatik, 2024).
- [50] E. Farhi and S. Gutmann, Analog analogue of a digital quantum computation, *Phys. Rev. A* **57**, 2403 (1998), *arXiv:quant-ph/9612026*.
- [51] A. J. Daley, I. Bloch, C. Kokail, S. Flannigan, N. Pearson,

- M. Troyer, and P. Zoller, Practical quantum advantage in quantum simulation, *Nature* **607**, 667 (2022).
- [52] J. S. Cotler, D. K. Mark, H.-Y. Huang, F. Hernández, J. Choi, A. L. Shaw, M. Endres, and S. Choi, Emergent quantum state designs from individual many-body wave functions, *PRX Quantum* **4**, 010311 (2023).
- [53] P. Hauke, M. Heyl, L. Tagliacozzo, and P. Zoller, Measuring multipartite entanglement through dynamic susceptibilities, *Nature Physics* **12**, 778–782 (2016).
- [54] X.-H. Deng, Y.-J. Hai, J.-N. Li, and Y. Song, Correcting correlated errors for quantum gates in multi-qubit systems using smooth pulse control, arXiv preprint arXiv:2103.08169 (2021).
- [55] Y.-J. Hai, S. Zhang, H. Guan, P. Huang, Y. He, and X.-H. Deng, Scalable robust quantum control for semiconductor spin qubits with always-on couplings (2025), arXiv:2503.12795 [quant-ph].
- [56] W. Cottrell, B. Freivogel, D. M. Hofman, and S. F. Lokhande, How to build the thermofield double state, *Journal of High Energy Physics* **2019**, 1 (2019).
- [57] J. M. Deutsch, Quantum statistical mechanics in a closed system, *Phys. Rev. A* **43**, 2046 (1991).
- [58] M. Srednicki, Chaos and quantum thermalization, *Phys. Rev. E* **50**, 888 (1994).
- [59] C. M. Bender and S. Boettcher, Real spectra in non-hermitian hamiltonians having PT symmetry, *Phys. Rev. Lett.* **80**, 5243 (1998).
- [60] C. M. Bender, D. C. Brody, H. F. Jones, and B. K. Meister, Faster than hermitian quantum mechanics, *Phys. Rev. Lett.* **98**, 040403 (2007).
- [61] N. Chakraborty, R. Moessner, and B. Douçot, Cross-platform protected qubits from entanglement, *Phys. Rev. B* **112**, 155111 (2025).
- [62] C. Ortiz Marrero, M. Kieferová, and N. Wiebe, Entanglement-induced barren plateaus, *PRX quantum* **2**, 040316 (2021).
- [63] T. L. Patti, K. Najafi, X. Gao, and S. F. Yelin, Entanglement devised barren plateau mitigation, *Phys. Rev. Res.* **3**, 033090 (2021).
- [64] N. Gleinig and T. Hoefler, An efficient algorithm for sparse quantum state preparation, in *2021 58th ACM/IEEE Design Automation Conference (DAC)* (IEEE, 2021) pp. 433–438.
- [65] X.-M. Zhang, T. Li, and X. Yuan, Quantum state preparation with optimal circuit depth: Implementations and applications, *Physical Review Letters* **129**, 10.1103/physrevlett.129.230504 (2022).
- [66] A. Osterloh, L. Amico, G. Falci, and R. Fazio, Scaling of entanglement close to a quantum phase transition, *Nature* **416**, 608 (2002).
- [67] T. J. Osborne and M. A. Nielsen, Entanglement in a simple quantum phase transition, *Phys. Rev. A* **66**, 032110 (2002).
- [68] S.-J. Gu, S.-S. Deng, Y.-Q. Li, and H.-Q. Lin, Entanglement and quantum phase transition in the extended hubbard model, *Phys. Rev. Lett.* **93**, 086402 (2004).
- [69] W. H. Zurek, Emergence of the classical world from within our quantum universe, in *From Quantum to Classical: Essays in Honour of H.-Dieter Zeh* (Springer, 2022) pp. 23–44.
- [70] J. Watrous, *The theory of quantum information* (Cambridge university press, 2018).
- [71] Y.-J. Hai, Y. Song, J. Li, J. Zeng, and X.-H. Deng, Geometric correspondence of noisy quantum dynamics and universal robust quantum gates, *Physical Review Applied* **23**, 054002 (2025).
- [72] H. Xue and X.-H. Deng, Quantum control robustness landscapes, in *2025 IEEE International Conference on Quantum Control, Computing and Learning (qCCL)* (IEEE, 2025) pp. 1–8.
- [73] G. Burkard, T. D. Ladd, A. Pan, J. M. Nichol, and J. R. Petta, Semiconductor spin qubits, *Reviews of Modern Physics* **95**, 025003 (2023).
- [74] K. Yi, Y.-J. Hai, K. Luo, J. Chu, L. Zhang, Y. Zhou, Y. Song, S. Liu, T. Yan, X.-H. Deng, *et al.*, Robust quantum gates against correlated noise in integrated quantum chips, *Physical Review Letters* **132**, 250604 (2024).
- [75] M. Russ, D. M. Zajac, A. J. Sigillito, F. Borjans, J. M. Taylor, J. R. Petta, and G. Burkard, High-fidelity quantum gates in si/sige double quantum dots, *Physical Review B* **97**, 085421 (2018).
- [76] U. Güngördü and J. Kestner, Robust implementation of quantum gates despite always-on exchange coupling in silicon double quantum dots, *Physical Review B* **101**, 155301 (2020).
- [77] D. W. Kanaar, S. Wolin, U. Güngördü, and J. Kestner, Single-tone pulse sequences and robust two-tone shaped pulses for three silicon spin qubits with always-on exchange, *Physical Review B* **103**, 235314 (2021).
- [78] I. Heinz, A. R. Mills, J. R. Petta, and G. Burkard, Analysis and mitigation of residual exchange coupling in linear spin-qubit arrays, *Physical Review Research* **6**, 013153 (2024).
- [79] M. T. Mađzik, S. Asaad, A. Youssry, B. Joecker, K. M. Rudinger, E. Nielsen, K. C. Young, T. J. Proctor, A. D. Baczewski, A. Laucht, *et al.*, Precision tomography of a three-qubit donor quantum processor in silicon, *Nature* **601**, 348 (2022).
- [80] Y. He, S. Gorman, D. Keith, L. Kranz, J. Keizer, and M. Simmons, A two-qubit gate between phosphorus donor electrons in silicon, *Nature* **571**, 371 (2019).

SUPPLEMENTARY MATERIALS OF "ENTANGLEMENT-INDUCED RESILIENCE OF QUANTUM DYNAMICS

Section A: General quantum dynamics of Time-dependent Hamiltonian with entanglement

By utilizing typical information about the states, one can achieve a more accurate quantification of the erroneous behaviors in quantum dynamics. We demonstrate that entanglement inherently provides a level of robustness against dynamic errors, allowing us to derive tighter and more reliable error analyses. This insight not only underscores the significance of entangled states in enhancing the fidelity of quantum simulations but also highlights the broader applicability.

Before exploring the role of entanglement in quantum dynamics, we introduce the following mathematical lemma:

Lemma 2. [44] *Let $A(t)$ and $B(t)$ be continuous time-dependent Hermitian operators, and let $U_A(t)$ and $U_B(t)$ with $U_A(0) = U_B(0) = I$ be the corresponding time evolution unitaries. Then $W(t) = U_B(t)^\dagger U_A(t)$ is the unique solution of $i\partial_t W(t) = U_B(t)^\dagger (A(t) - B(t)) U_B(t) W(t)$, and $W(0) = I$.*

Now suppose $A(t) = H_0(t)$ is the ideal Hamiltonian and $B(t) = H'(t)$ which is the noisy Hamiltonian, we have $W(t) = U_B(t)^\dagger U_A(t) = \mathcal{T} e^{\int_{s_1=0}^t ds_1 i H'(s_1)} \mathcal{T} e^{-\int_{s_2=0}^t ds_2 i H_0(s_2)}$. Note that we would like to quantify the distance between $U_A(t)$ and $U_B(t)$ with initial state $|\psi\rangle$. By making use of Lemma 2, we now have

$$\begin{aligned}
\|(U_A(t) - U_B(t)) |\psi\rangle\| &= \|U_B(t)(W(t) - I) |\psi\rangle\| \\
&= \|(W(t) - I) |\psi\rangle\| \\
&= \|(W(t) - W(0)) |\psi\rangle\| \\
&= \left\| i \int_0^t dt \partial_\tau W(\tau) |\psi\rangle \right\| \\
&= \left\| \left[\int_0^t d\tau U_B(\tau)^\dagger (A(\tau) - B(\tau)) U_B(\tau) W(\tau) \right] |\psi\rangle \right\| \\
&= \left\| \left[\int_0^t d\tau U_B(\tau)^\dagger (A(\tau) - B(\tau)) U_A(\tau) \right] |\psi\rangle \right\| \tag{A1} \\
&\leq \int_0^t d\tau \left\| [(A(\tau) - B(\tau)) U_A(\tau)] |\psi\rangle \right\| \\
&= \int_0^t d\tau \left\| [H'(\tau) - H_0(\tau)] e^{-\int_s^\tau ds i H(s)} |\psi\rangle \right\| \\
&= \int_0^t d\tau \left\| [H'(\tau) - H_0(\tau)] |\psi(\tau)\rangle \right\|.
\end{aligned}$$

Here we have use $\|UA|\psi\rangle\| = \|A|\psi\rangle\|$ since U is unitary. One can see that the error term of the upper bound now becomes $H'(\tau) - H_0(\tau)$ in the case of a time-dependent Hamiltonian, where $|\psi(\tau)\rangle$ is the ideal evolved state for evolution time τ . We now summarise the above result as the following Corollary:

Corollary 1 (Bound on the difference between evolved states with time-dependent Hamiltonians). *Let $|\psi(0)\rangle$ be an initial state, and consider two time-dependent Hamiltonians $H_0(\tau)$ and $H'(\tau)$. The vector norm of the difference of two evolved states satisfies*

$$\left\| \left(\mathcal{T} e^{-i \int_0^t d\tau H_0(\tau)} - \mathcal{T} e^{-i \int_0^t d\tau H'(\tau)} \right) |\psi(0)\rangle \right\| \leq \int_0^t d\tau \left\| [H'(\tau) - H_0(\tau)] |\psi(\tau)\rangle \right\|, \tag{A2}$$

where \mathcal{T} denotes time-ordering and $|\psi(\tau)\rangle$ is the state evolved under the Hamiltonian $H'(\tau)$.

This corollary provides a quantitative measure of how differences in the Hamiltonians influence the evolution of the quantum state over time.

1. Entanglement-based bound of quantum dynamics

Here, we investigate how entanglement influences the upper bound of error for general quantum dynamics.

Time-independent perturbation. Suppose $H'(\tau) = H(\tau) + H_{\text{pert}}$ and H_{pert} is time-independent and $H_{\text{pert}} = \sum_k \delta_k V_k + \sum_m \eta_m N_m = \sum_j H_{\text{pert}_j}$ where V_k and N_m are Pauli operators. Note that H_{pert} is Hermitian, thus we have

$$\begin{aligned}
\|(U_A(t) - U_B(t))|\psi\rangle\| &\leq \int_0^t d\tau \| [H'(\tau) - H_0(\tau)] |\psi(\tau)\rangle \| \\
&= \int_0^t d\tau \| H_{\text{pert}} |\psi(\tau)\rangle \| \\
&= \int_0^t d\tau \sqrt{\langle \psi(\tau) | H_{\text{pert}}^\dagger H_{\text{pert}} | \psi(\tau) \rangle} \\
&\leq \int_0^t d\tau \sqrt{\|H_{\text{pert}}\|_F^2 + \sum_{j,j'} \|H_{\text{pert}_j}^\dagger H_{\text{pert}_{j'}}\| \sqrt{2 \log(d_{\text{supp}(H_{\text{pert}_j}^\dagger H_{\text{pert}_{j'}})}) - 2S(\rho_{j,j'})}} \\
&\leq t \|H_{\text{pert}}\|_F + \int_0^t d\tau \sqrt{\sum_{j,j'} \|H_{\text{pert}_j}^\dagger H_{\text{pert}_{j'}}\| \sqrt{2 \log(d_{\text{supp}(H_{\text{pert}_j}^\dagger H_{\text{pert}_{j'}})}) - 2S(\rho_{j,j'})}},
\end{aligned} \tag{A3}$$

where $\rho_{j,j'} := \text{Tr}_{[N] \setminus \text{supp}(H_{\text{pert}_j}^\dagger H_{\text{pert}_{j'}})}(|\psi\rangle\langle\psi|)$ is the reduced density matrix of $|\psi\rangle\langle\psi|$ on the subsystem of $\text{supp}(H_{\text{pert}_j}^\dagger H_{\text{pert}_{j'}})$, and $S(\rho_{j,j'})$ is the entanglement entropy of $\rho_{j,j'}$. Here $\|\cdot\|_F$ denotes the normalized Frobenius norm, and in the penultimate inequality, we have utilized the Lemma 4 while the final inequality we make use of $\sqrt{a+b} \leq \sqrt{a} + \sqrt{b}$ for positive semi-definite a and b .

Generally, states tend to be thermalized. Suppose $t = c$, state entanglement is growing to approximate the average case, and $\tau \geq c$, $\|H_{\text{pert}}|\psi(\tau)\rangle\| \approx \|H_{\text{pert}}\|_F$. In this case, we have

$$\|(U_A(t) - U_B(t))|\psi\rangle\| \lesssim \int_0^c d\tau \sqrt{\langle \psi(\tau) | H_{\text{pert}}^\dagger H_{\text{pert}} | \psi(\tau) \rangle} + (t - c) \|H_{\text{pert}}\|_F. \tag{A4}$$

For the average case (Haar random or 1 design), we have

$$\begin{aligned}
\int_{\psi \in \text{Haar}} d\psi \|(U_0(t) - U(t))|\psi\rangle\| &\leq \int_{\psi \in \text{Haar}} d\psi \int_0^t d\tau \sqrt{\langle \psi(\tau) | H_{\text{pert}}^\dagger H_{\text{pert}} | \psi(\tau) \rangle} \\
&\leq \int_0^t d\tau \sqrt{\int_{\psi \in \text{Haar}} d\psi \langle \psi(\tau) | H_{\text{pert}}^\dagger H_{\text{pert}} | \psi(\tau) \rangle} \\
&= \int_0^t d\tau \sqrt{\text{Tr}\left(\frac{H_{\text{pert}}^\dagger H_{\text{pert}}}{d}\right)} = t \|H_{\text{pert}}\|_F.
\end{aligned} \tag{A5}$$

Thus, our entanglement-induced bound matches the average case when $t \geq c$.

Remarkably, there is a special case where the worst case is equal to the average case, i.e., the spectral norm $\|H_{\text{pert}}\|$ is equal to the normalized Frobenius norm $\|H_{\text{pert}}\|_F$. Specifically, suppose $H_{\text{pert}}^\dagger H_{\text{pert}} = \beta I$ and it is easy to prove that $\beta = \|H_{\text{pert}}\|_F^2 = \|H_{\text{pert}}\|^2$. In this case, the upper bound of state error becomes

$$\begin{aligned}
\|(U_A(t) - U_B(t))|\psi\rangle\| &\leq \int_0^t d\tau \lambda \sqrt{\langle \psi(\tau) | H_{\text{pert}}^\dagger H_{\text{pert}} | \psi(\tau) \rangle} \\
&= \int_0^t d\tau \lambda \sqrt{\beta} \sqrt{\langle \psi(\tau) | I | \psi(\tau) \rangle} = t \|H_{\text{pert}}\|_F.
\end{aligned} \tag{A6}$$

In this case, the upper bound of error is independent of any states and achieve the average case performance. One of the sufficient conditions for $H_{\text{pert}}^\dagger H_{\text{pert}} = \beta I$, is each pair of H_{pert_i} and H_{pert_j} ($i \neq j$) satisfies $\{H_{\text{pert}_i}, H_{\text{pert}_j}\} = 0$.

Time-dependent perturbation. In general, $H_{\text{pert}} = H'(\tau) - H_0(\tau)$ may be time-dependent, e.g., $H_{\text{pert}} = H_{\text{pert}}(\tau)$. Here for investigate how entanglement plays the role in the error bound of the time-dependent cases, we define $\Delta t = t/J$ and rewrite the upper bound as

$$\|(U_A(t) - U_B(t))|\psi\rangle\| \leq \int_0^t d\tau \|H_{\text{pert}}(\tau)|\psi(\tau)\rangle\| = \sum_{j=0}^{J-1} \int_{j\Delta t}^{(j+1)\Delta t} d\tau \sqrt{\langle\psi(\tau)|H_{\text{pert}}^\dagger(\tau)H_{\text{pert}}(\tau)|\psi(\tau)\rangle}. \quad (\text{A7})$$

Note that $\|H_{\text{pert}}|\psi(\tau)\rangle\|^2 \leq \|H_{\text{pert}}(\tau)\|_F^2 + \Delta_{H_{\text{pert}}^\dagger(\tau)H_{\text{pert}}(\tau)}(\psi(\tau))$ (see Eq. (A3)) where

$$\Delta_{H_{\text{pert}}^\dagger(\tau)H_{\text{pert}}(\tau)}(\psi(\tau)) = \sum_{j,j'} \left\| H_{\text{pert}_j}^\dagger(\tau)H_{\text{pert}_{j'}}(\tau) \right\| \sqrt{2 \log \left(d_{\text{supp}(H_{\text{pert}_j}^\dagger(\tau)H_{\text{pert}_{j'}}(\tau))} - 2S(\rho_{j,j'}) \right)}.$$

Define $A_{j\Delta t}^{(j+1)\Delta t} = \int_{j\Delta t}^{(j+1)\Delta t} d\tau H_{\text{pert}}^\dagger(\tau)H_{\text{pert}}(\tau)$, a positive operator for segment j , we bound the error as

$$(\Delta t)^{\frac{1}{2}} \sum_{j=0}^{J-1} \sqrt{\frac{\text{Tr}(A_{j\Delta t}^{(j+1)\Delta t})}{d}} + \sum_{j=0}^{J-1} \int_{j\Delta t}^{(j+1)\Delta t} d\tau \sqrt{\Delta_{H_{\text{pert}}^\dagger(\tau)H_{\text{pert}}(\tau)}(\psi(\tau))}. \quad (\text{A8})$$

We have make use of the inequality $\sqrt{x^2 + y^2} \leq x + y$ for positive numbers x and y , and the Cauchy-Schwarz inequality $\int_a^b f(x)g(x)dx \leq \sqrt{\int_a^b f^2(x)dx} \sqrt{\int_a^b g^2(x)dx}$. Suppose $|\psi\rangle(\tau)$ have enough entanglement all the time, one has

$$\|(U_A(t) - U_B(t))|\psi\rangle\| \lesssim \sum_{j=0}^{J-1} (\Delta t)^{\frac{1}{2}} \sqrt{\frac{\text{Tr}(A_{j\Delta t}^{(j+1)\Delta t})}{d}} = \int_0^t \|H_{\text{pert}}(\tau)\|_F. \quad (\text{A9})$$

It is easy to verify that, if $H_{\text{pert}}(\tau) = H_{\text{pert}}$, one has $A_{j\Delta t}^{(j+1)\Delta t} = \Delta t H_{\text{pert}}^\dagger H_{\text{pert}}$, and the Eq. (A8) can reduce to

$$t \|H_{\text{pert}}\|_F + \int_0^t d\tau \sqrt{\Delta_{H_{\text{pert}}^\dagger(\tau)H_{\text{pert}}(\tau)}(\psi(\tau))}, \quad (\text{A10})$$

which is the exact upper bound of the total error for the time-independent perturbation case.

2. Trace distance with statistical disorder

The statistical properties of δ_k may further cancel some errors in quantum dynamics. Recall that $H_{\text{pert}} = \sum_k \delta_k V_k + \sum_m \eta_m N_m$ and δ_k is the random real parameter of Gaussian distribution. Assuming that the Gaussian distribution has $\mathbb{E}\delta_k = 0$ and $\text{Var}(\delta_k) = \sigma_k^2$. Note that the upper bounds of the above analysis are for a single run with fixed δ_k . By considering the unbiased perturbative nature of δ_k , the density matrix of the real evolved state is given as

$$\rho(t) = \mathbb{E}_{\{\delta_1, \delta_2, \dots\}} U(t) |\psi\rangle \langle\psi| U^\dagger(t),$$

where $U(t) = \mathcal{T} e^{-i \int H'(t) dt}$ and $H' = H_0 + H_{\text{pert}}$. Now, the distance between the ideal evolution and the approximated one should be defined by the 1-norm $\|\rho_0(t) - \rho(t)\|_1$ ($\|A\|_1 = \text{Tr}(\sqrt{A^\dagger A})$), not the vector norm. Here $\rho_0(t) = U_0(t) |\psi\rangle \langle\psi| U_0^\dagger(t)$.

The trace distance between the ideal evolution state and the approximate evolution state is

$$\begin{aligned} \|\rho_0(t) - \rho(t)\|_1 &= \|U_0(t) |\psi\rangle \langle\psi| U_0^\dagger(t) - \mathbb{E}_{\{\delta_1, \delta_2, \dots\}} U(t) |\psi\rangle \langle\psi| U^\dagger(t)\|_1 \\ &\leq \mathbb{E}_{\{\delta_1, \delta_2, \dots\}} \|U_0(t) |\psi\rangle \langle\psi| U_0^\dagger(t) - U(t) |\psi\rangle \langle\psi| U^\dagger(t)\|_1 \\ &\leq 2 \mathbb{E}_{\{\delta_1, \delta_2, \dots\}} \|(U_0(t) - U(t))|\psi\rangle\| \\ &\leq 2 \mathbb{E}_{\{\delta_1, \delta_2, \dots\}} \int_0^t d\tau \sqrt{\langle\psi(\tau)|H_{\text{pert}}^\dagger H_{\text{pert}}|\psi(\tau)\rangle} \\ &\leq 2 \int_0^t d\tau \sqrt{\langle\psi(\tau)|\mathbb{E}_{\{\delta_1, \delta_2, \dots\}} H_{\text{pert}}^\dagger H_{\text{pert}}|\psi(\tau)\rangle}. \end{aligned} \quad (\text{A11})$$

For the first inequality, we use the triangle inequality. For the second inequality, for any two projectors $|\chi\rangle\langle\chi|$ and $|\phi\rangle\langle\phi|$, the following inequality holds, e.g., $\| |\chi\rangle\langle\chi| - |\phi\rangle\langle\phi| \|_1 \leq 2\| |\psi\rangle - |\phi\rangle \|$. In the last inequality, we utilize the Cauchy-Schwarz inequality.

Generally, $H_{\text{pert}} = V + N = \sum_k \delta_k V_k + \sum_m \eta_m N_m$, one has

$$\begin{aligned}
\mathbb{E}_{\{\delta_1, \delta_2, \dots\}} H_{\text{pert}}^\dagger H_{\text{pert}} &= \mathbb{E}_{\{\delta_1, \delta_2, \dots\}} \left(\sum_k \delta_k V_k + \sum_m \eta_m N_m \right)^\dagger \left(\sum_{k'} \delta_{k'} V_{k'} + \sum_{m'} \eta_{m'} N_{m'} \right) \\
&= \mathbb{E}_{\{\delta_1, \delta_2, \dots\}} \left(\sum_{k, k'} \delta_k \delta_{k'} V_k^\dagger V_{k'} + \sum_{k, m'} \delta_k \eta_{m'} V_k^\dagger N_{m'} + \sum_{m, k'} \eta_m \delta_{k'} N_m^\dagger V_{k'} + \sum_{m, m'} \eta_m \eta_{m'} N_m^\dagger N_{m'} \right) \\
&= \mathbb{E}_{\{\delta_1, \delta_2, \dots\}} \sum_{k, k'} \delta_k \delta_{k'} V_k^\dagger V_{k'} + \sum_{m, m'} \eta_m \eta_{m'} N_m^\dagger N_{m'} \\
&= \mathbb{E}_{\{\delta_1, \delta_2, \dots\}} \sum_k \delta_k^2 V_k^\dagger V_k + \sum_{m, m'} \eta_m \eta_{m'} N_m^\dagger N_{m'} \\
&= \mathbb{E}_{\{\delta_1, \delta_2, \dots\}} \sum_k \delta_k^2 V_k^\dagger V_k + N^\dagger N.
\end{aligned} \tag{A12}$$

Suppose $\{V_k\}$ are Pauli operators (up to a global phase),

$$\mathbb{E}_{\{\delta_1, \delta_2, \dots\}} H_{\text{pert}}^\dagger H_{\text{pert}} = \mathbb{E}_{\{\delta_1, \delta_2, \dots\}} \sum_k \delta_k^2 I + N^\dagger N. \tag{A13}$$

Now the distance of the quantum state is given as

$$\begin{aligned}
\|\rho_0(t) - \rho(t)\|_1 &\leq 2 \int_0^t d\tau \sqrt{\langle \psi(\tau) | \mathbb{E}_{\{\delta_1, \delta_2, \dots\}} (H_{\text{pert}}^\dagger H_{\text{pert}}) | \psi(\tau) \rangle} \\
&= 2 \int_0^t d\tau \sqrt{\langle \psi(\tau) | (\mathbb{E}_{\{\delta_1, \delta_2, \dots\}} \sum_k \delta_k^2 I + N^\dagger N) | \psi(\tau) \rangle} \\
&= 2 \int_0^t d\tau \sqrt{\mathbb{E}_{\{\delta_1, \delta_2, \dots\}} \sum_k \delta_k^2 + \langle \psi(\tau) | N^\dagger N | \psi(\tau) \rangle} \\
&= 2 \int_0^t d\tau \sqrt{\sum_k \sigma_k^2 + \langle \psi(\tau) | N^\dagger N | \psi(\tau) \rangle}, \\
&\leq 2t \sqrt{\sum_k \sigma_k^2} + 2 \int_0^t d\tau \sqrt{\langle \psi(\tau) | N^\dagger N | \psi(\tau) \rangle},
\end{aligned} \tag{A14}$$

where $\sigma_k = \delta_k^2$ is the variance of the Gaussian distribution. Eventually, one has the entanglement-based bound for the density matrix case, i.e.,

$$\|\rho_0(t) - \rho(t)\|_1 \leq 2t \sqrt{\sum_k \sigma_k^2} + 2t \|N\|_F + 2 \int_0^t \tau \sqrt{\Delta_{N^\dagger N}(\psi(\tau))}, \tag{A15}$$

where $\Delta_{N^\dagger N}(\psi(\tau)) = \sum_{j, j'} \|N_j^\dagger N_{j'}\| \sqrt{2 \log \left(d_{\text{supp}(N_j^\dagger N_{j'})} \right) - 2S(\rho_{j, j'}(\tau))}$.

Section B: The entanglement role in quantum control

In this section, we specifically focus on the quantum control with an entangled input state, which is ubiquitous in the realm of quantum many-body physics. We demonstrate that entanglement inherently provides a level of robustness against quantum control errors, allowing us to derive tighter and more reliable error analyses.

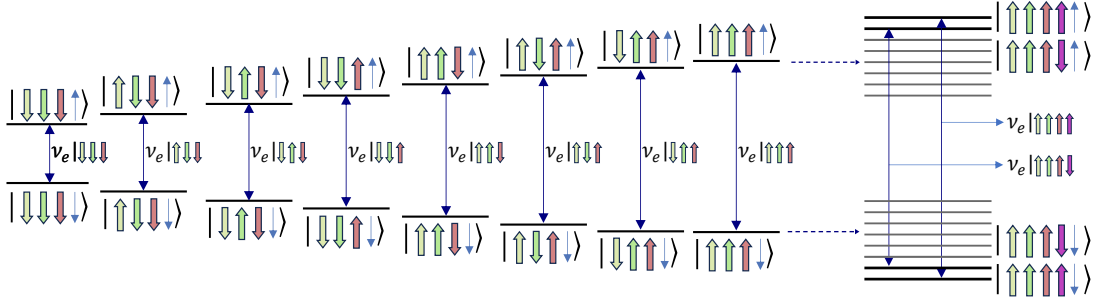


FIG. 8: Spectator-induced energy-level splitting. The interaction between the target-controlled qubit and spectators causes the energy levels to split into energy bands. As a result, the spectators lead to unavoidable errors in the implementation of a quantum gate.

Suppose one wants to implement a k -qubit quantum gate. In general, the k target qubit is coupled to neighboring qubits (spectators or intruders). The total Hamiltonian with physical basis can be expressed as $\tilde{H} = \tilde{H}_0 + \tilde{V}(t)$ where \tilde{H}_0 is the native Hamiltonian and $\tilde{V}(t)$ is the control field. To analyze coupling effects in the eigenbasis of \tilde{H}_0 , the Hamiltonian can be decomposed into blocks [55]

$$H^{m;k} = \bigoplus_{i=1}^{2^m} H_i + \bigoplus_{i,j=1}^{2^m} V_{ij}(t) = \begin{pmatrix} H_1 + V_{11} & V_{12} & \dots & V_{1m} \\ V_{12}^\dagger & H_2 + V_{22} & \dots & V_{2m} \\ \dots & \dots & \dots & \dots \\ V_{1m}^\dagger & V_{2m}^\dagger & \dots & H_m + V_{mm} \end{pmatrix}. \quad (\text{B1})$$

Here, the superscript $m; d$ denotes a system with m neighboring qubits affecting k target qubits. The Hamiltonian decomposes into $2^m \times 2^m$ blocks corresponding to different configurations of the neighboring qubits. For example, in a system with two neighboring qubits and one target qubit, $\text{span}\{|\uparrow\uparrow; \uparrow\rangle, |\uparrow\uparrow; \downarrow\rangle\}$ represents the $i = 1$ diagonal subspace where both neighboring qubits are in the $|\uparrow\rangle$ state.

Without loss of generality, we designate the $i = 1$ subspace as our reference and define the reference Hamiltonian $H_{\text{ref}} = H_1 + V_{11}$. The difference between the reference and the original Hamiltonian is identified as the noise Hamiltonian:

$$H_{\text{noise}} = H^{m;k} - H_{\text{ref}} = \bigoplus_{i=2}^{2^m} (\Delta H_i + \Delta V_{ii}) + \bigoplus_{i,j=1, i \neq j}^{2^m} V_{ij} = \begin{pmatrix} 0 & V_{12} & \dots & V_{1m} \\ V_{12}^\dagger & \Delta H_2 + \Delta V_{22} & \dots & V_{2m} \\ \dots & \dots & \dots & \dots \\ V_{1m}^\dagger & V_{2m}^\dagger & \dots & \Delta H_m + \Delta V_{mm} \end{pmatrix} \quad (\text{B2})$$

Here, $\Delta H_i = H_i - H_1$ represents frequency shifts experienced by target qubits due to different configurations of neighboring qubits, collectively forming a manifold of 2^m distinct energy levels (as shown in Figure 8). The terms $\Delta V_{ii} = V_{ii} - V_{11}$ represent variations in control field effects across different neighboring-qubit configurations, while $V_{ij}(t)$ for $i \neq j$ captures crosstalk between different subspaces. These noise terms introduce correlated errors, parasitic operations, and cross-coupling effects that degrade gate fidelities.

1. Error analysis of quantum control with a single two-party partition

Recall that H_{error} is time-dependent in quantum control protocols, e.g, $H_{\text{error}} = H_{\text{error}}(\tau)$. Here, for simplicity to show the important role of entanglement in quantum control, we treat $H_{\text{error}}^\dagger(\tau)H_{\text{error}}(\tau)$ as a single term. Denote A as the subsystem of target qubits and spectators, and B as the remaining qubits. In this setting, $H_{\text{error}}^\dagger(\tau)H_{\text{error}}(\tau)$ can be consider a local error term in the subsystems A . Now, by using Lemma 4 (single term case), the error upper bound of the implementation of a quantum gate with state $|\psi(0)\rangle = |\psi(0)\rangle_{AB}$ is given as

$$\begin{aligned}
\|(U_0(t) - U(t)) |\psi(0)\rangle_{AB}\| &\leq \int_0^t d\tau \sqrt{\langle \psi(\tau) |_{AB} H_{\text{error}}^\dagger(\tau) H_{\text{error}}(\tau) | \psi(\tau) \rangle_{AB}} \\
&\leq \int_0^t d\tau \sqrt{\|H_{\text{error}}\|_F^2 + \|H_{\text{error}}^\dagger H_{\text{error}}\| \sqrt{2(\log d_A - S(\rho_A(\tau)))}} \\
&\leq \int_0^t d\tau \|H_{\text{error}}(\tau)\|_F + \int_0^t \sqrt{\|H_{\text{error}}^\dagger(\tau) H_{\text{error}}(\tau)\| \sqrt{2(\log d_A - S(\rho_A(\tau)))}}.
\end{aligned} \tag{B3}$$

In the main text, we trace the upper bound of quantum gate error with quantum control by $\int_0^t d\tau \sqrt{\langle \psi(\tau) | H_{\text{error}}^\dagger H_{\text{error}} | \psi(\tau) \rangle}$. For the modest system sizes considered in quantum control protocols, this quantity can be calculated efficiently. Clearly, if the entanglement of $|\psi(\tau)\rangle_{AB}$ is large enough at the period of quantum control, one has $\|(U_0(t) - U(t)) |\psi\rangle\| \approx \int_0^t d\tau \|H_{\text{error}}(\tau)\|_F$.

It is important to note that entanglement can also occur between the target qubits and the nearby spectators within subsystem A, which can contribute to noise suppression. To clearly and simply demonstrate the role of entanglement in quantum control, we categorize these interactions into a single class, e.g., treating the target and spectators as a subsystem, rather than subdividing them into many subspaces composed of error terms $H_{\text{error}}(\tau)_j$.

2. Error analysis with interaction picture

To more intuitive to show how entanglement suppress the evolved state error after evolution, one can decompose the total evolution operator as $U = U_0 U_e$, separating the ideal evolution $U_0(t) = \mathcal{T} \exp\{-i \int_0^t d\tau H_{\text{ref}}(\tau)\}$ from the error evolution $U_e(t) = \mathcal{T} \exp\{-i \int_0^t d\tau V_I(\tau)\}$. Here, $V_I = U_0^\dagger H_{\text{error}} U_0$ represents the noise Hamiltonian in the interaction picture. For any operator K , we define the super-operator $\mathcal{R}(K(t)) = \int_0^t d\tau U_0(\tau)^\dagger K(\tau) U_0(\tau)$, which represents the time-integrated effect of K as transformed by the ideal evolution. In the Pauli basis $\{\sigma_\nu^k\} = \{X, Y, Z, I\}^{\otimes k}$, an operator $K = \mathbf{T} \cdot \sigma^k$ can be conceptualized as a point moving with velocity \mathbf{T} in operator space, and $\mathcal{R}(K(t)) = \mathbf{r} \cdot \sigma^k$ represents the integrated path traced by this point in the Pauli frame [71].

Under the assumption that the noise terms are small in comparison to the ideal Hamiltonian, one can employ the first-order Magnus expansion to eliminate time-ordering, resulting in a product of error evolution operators corresponding to each error term. Additionally, we applied the first order of the Taylor series to derive:

$$\begin{aligned}
U_e(t) &= \mathcal{T} \exp\{-i \mathcal{R} H_{\text{error}}(t)\} \approx \prod_{j,k=1}^{2^m} e^{-i \mathcal{R}(\Delta H_j)} e^{-i \mathcal{R}(\Delta V_j)} e^{-i \mathcal{R}(V_{jk})} \\
&\approx I - i \sum_{\mu} \mathcal{R}(K_{\mu}) = I - i \sum_{\mu} \mathbf{r}_{\mu}(t) \cdot \sigma^{m+k},
\end{aligned} \tag{B4}$$

where each noise term K_{μ} belongs to the set $\{\Delta H_j, \Delta V_j, V_{jl}\}$. Each error component generates an error curve $\mathbf{r}_{\mu}(t)$ in operator space, with the vector norm $\|\mathbf{r}_{\mu}(t)\|$ quantifying the magnitude of the associated error. Note that here σ^k denotes the Pauli operator for the target k qubits.

Recall that $U_e(t) = I + \mathcal{M}(t) \approx I_{md} - i \sum_{\mu} \mathbf{r}_{\mu}(t) \cdot \sigma^{m+k}$, now the additive error of the ideal unitary $U_0(t)$ and the approximate unitary $U(t) = U_0(t) U_e(t)$ for given initial state $|\psi\rangle$ is given as

$$\begin{aligned}
\|(U_0(t) - U(t)) |\psi\rangle\| &= \|U_0(t)(I - U_e) |\psi\rangle\| \\
&\approx \left\| U_0(t) \left(i \sum_{\mu} \mathbf{r}_{\mu}(t) \cdot \sigma^{m+k} \right) |\psi\rangle \right\| = \left\| \left(\sum_{\mu} \mathbf{r}_{\mu}(t) \cdot \sigma^{m+k} \right) |\psi\rangle \right\|.
\end{aligned} \tag{B5}$$

The average error is bounded by

$$\begin{aligned}
\int_{\psi \in \text{Haar}} d\psi \| (U_0(t) - U(t)) |\psi\rangle \| &\approx \int_{\psi \in \text{Haar}} d\psi \left\| \left(\sum_{\mu} \mathbf{r}_{\mu}(t) \cdot \sigma^{k+m} \right) |\psi\rangle \right\| \\
&= \int_{\psi \in \text{Haar}} d\psi \sqrt{\langle \psi | \left(\sum_{\mu'} \mathbf{r}_{\mu'}(t) \cdot \sigma^{k+m} \right)^\dagger \left(\sum_{\mu} \mathbf{r}_{\mu}(t) \cdot \sigma^{k+m} \right) | \psi \rangle} \\
&\leq \sqrt{\int_{\psi \in \text{Haar}} d\psi \langle \psi | \left(\sum_{\mu'} \mathbf{r}_{\mu'}(t) \cdot \sigma^{k+m} \right)^\dagger \left(\sum_{\mu} \mathbf{r}_{\mu}(t) \cdot \sigma^{k+m} \right) | \psi \rangle} \\
&= \sqrt{\text{Tr} \left[\left(\sum_{\mu'} \mathbf{r}_{\mu'}(t) \cdot \sigma^{m+k} \right)^\dagger \left(\sum_{\mu} \mathbf{r}_{\mu}(t) \cdot \sigma^{m+k} \right) \right] / d} \\
&= \left\| \sum_{\mu} \mathbf{r}_{\mu}(t) \cdot \sigma^{m+k} \right\|_F.
\end{aligned} \tag{B6}$$

In the above inequality, we use the 1-design properties of Haar-random. This suggests our analysis holds for 1-design ensembles.

In quantum control theory, one usually defines the total error distance as a measure of control robustness against all noises

$$D = 2^{-\frac{m+k}{2}} \sum_{\mu} \|\mathbf{r}_{\mu} \cdot \sigma^{m+k}\|_2 = \sum_{\mu} \|\mathbf{r}_{\mu}(t)\|. \tag{B7}$$

Here $\|\cdot\|_2$ denotes the 2 norm or unnormalized Frobenius norm. Since $\left\| \sum_{\mu} \mathbf{r}_{\mu}(t) \cdot \sigma^{m+k} \right\|_F \leq \sum_{\mu} \|\mathbf{r}_{\mu}(t)\|$, this measure is the upper bound of the average performance of multiplicate error for random input states. It also suggests that the transitional bound of quantum control is not tight in the average case (note that this distance is not the worst case either).

For perfect gate implementation with high precision and robustness, we require $U_0(T) = U_{\text{target}}$ or the noiseless gate fidelity and error distance $D = 0$. Therefore, the error upper bound serves as the error-correcting constraint when designing robust control pulses [72]. Here, we show that, in the case of an input state that has sufficient entanglement between the target qubits and the remaining qubits, the error of implementing the target unitary can be reduced to the random case. Since $\|(U_0(t) - U(t)) |\psi\rangle\| \approx \left\| \left(\sum_{\mu} \mathbf{r}_{\mu}(t) \cdot \sigma^{m+k} \right) |\psi\rangle \right\|$, by utilizing our entanglement-based lemma, we have

$$\|(U_0(t) - U(t)) |\psi\rangle\| \approx \left\| \sum_{\mu} \mathbf{r}_{\mu}(t) \cdot \sigma^{m+k} \right\|_F. \tag{B8}$$

This suggests that entanglement can induce robustness in implementing quantum gates.

3. Quantum control of coupled quantum dots

To illustrate our approach, we consider a common example: a pair of coupled gate-defined quantum dots. The spin states follow an extended Heisenberg Hamiltonian [73]

$$\tilde{H} = \sum_i \mathbf{B}_i \cdot \mathbf{S}_i + \sum_{\langle i,j \rangle} J \left(\mathbf{S}_i \cdot \mathbf{S}_j - \frac{1}{4} \right). \tag{B9}$$

Here, $\mathbf{S}_j = (S_{Xj}, S_{Yj}, S_{Zj})/2$ are the spin operators, and $\mathbf{B}_j = (B_{x,j}, B_{y,j}, B_{z,j})$ represents the magnetic field at each qubit. The z-components of the magnetic fields determine the electron spin resonance frequencies, while transverse fields provide qubit control. The exchange coupling J brings the two spins into the coupled basis $\{|\uparrow\uparrow\rangle, |\tilde{\uparrow}\downarrow\rangle, |\downarrow\uparrow\rangle, |\downarrow\downarrow\rangle\}$, in which the Hamiltonian without transverse controls is diagonalized as $\tilde{H}_0 = \text{diag}\{2E_z, -\Delta\tilde{E}_z - J, \Delta\tilde{E}_z - J, -2E_z\}$, where $\Delta\tilde{E}_z = \sqrt{J^2 + \Delta E_z^2}$, $|\tilde{\uparrow}\downarrow\rangle = \cos\theta |\uparrow\downarrow\rangle + \sin\theta |\downarrow\uparrow\rangle$, $|\downarrow\uparrow\rangle = \sin\theta |\uparrow\downarrow\rangle + \cos\theta |\downarrow\uparrow\rangle$, and $\tan\theta = \frac{J}{\Delta E_z + \Delta\tilde{E}_z}$.

When driving qubit 2 with a transverse field and transforming to the rotating frame, we obtain

$$H^{1;1} = \begin{pmatrix} \tilde{H}_1 + \tilde{V}_{11} & \tilde{V}_{12} \\ \tilde{V}_{21} & \tilde{H}_2 + \tilde{V}_{22} \end{pmatrix}, \quad (\text{B10})$$

where the components are given by $H_{1,2} = \text{diag}\{\pm J/4, \mp J/4\}$, $\tilde{V}_{11} = \tilde{V}_{22} = \frac{\Omega_2}{2}X$, $\tilde{V}_{12,21} = \frac{1}{2}e^{\pm i\tilde{E}_z t} \tan \theta \Omega_2 Z$. In the coupled Pauli basis, it is simplified as

$$H^{1;1} = \frac{\Omega_2(t)}{2}IX + \frac{J}{4}ZZ + \frac{\tan \theta \Omega_2(t)}{2} \times \left[\cos(\Delta \tilde{E}_z t)XZ - \sin(\Delta \tilde{E}_z t)YZ \right]. \quad (\text{B11})$$

This Hamiltonian contains the intended control term (IX) along with parasitic terms: always-on ZZ coupling and crosstalk terms (XZ, YZ). Besides the coupling-induced terms, the total noise Hamiltonian also includes frequency drifts δ and control amplitude fluctuations ϵ [74]. Hence, the total perturbation Hamiltonian is

$$H_{\text{pert}}^{1,1} = \delta IZ + \delta ZI + \epsilon \Omega_2(t)IX + \frac{J}{4}ZZ + \frac{\tan \theta \Omega_2(t)}{2} \left[\cos(\Delta \tilde{E}_z t)XZ - \sin(\Delta \tilde{E}_z t)YZ \right]. \quad (\text{B12})$$

This perturbative term can be generalized to the multi-spectator case. Given $\{m, 1\}$ spectators and target qubits, the total perturbation Hamiltonian that induces errors on the target qubit is

$$H_{\text{pert}}^{m,1} = \sum_i \delta Z_i + \epsilon \Omega_2(t)X_1 + \sum_i \frac{J}{4}Z_i Z_1 + \sum_i \frac{\tan \theta \Omega_2(t)}{2} \left[\cos(\Delta \tilde{E}_z t)X_i Z_1 - \sin(\Delta \tilde{E}_z t)Y_i Z_1 \right]. \quad (\text{B13})$$

In experimentally relevant regimes where $J \ll \Delta E_z$, we consider $J/\Delta E_z < 0.1$ and get $\tan \theta \approx J/2\Delta E_z$. The magnitudes of crosstalk noise and always-on coupling scale as $|\tan \theta \Omega_2|$ and J , respectively. While crosstalk is often negligible in weak-drive regimes [75–77], it becomes significant under strong-drive conditions needed for fast gate operations, thereby necessitating the simultaneous suppression of both error channels [78, 79] for high-fidelity operations in multi-qubit systems.

4. Two-qubit gate with quantum control

For a two-qubit gate, $\{m, 2\}$ indicates two target qubits and m spectators, depending on lattice geometry. For example, in a square lattice, $m = 6$. The Hamiltonian to implement a \sqrt{SWAP} gate [80] in the raw basis (computational basis) relies on the standard homogeneous Heisenberg interaction $\tilde{H} = \sum_i \mathbf{B} \cdot \mathbf{S}_i + \sum_{\langle i,j \rangle} J(\mathbf{S}_i \cdot \mathbf{S}_j - \frac{1}{4})$ by taking $\mathbf{B}_1 = \mathbf{B}_2$. Correspondingly, the entangling gate is $U = \text{diag}\{1, -1, 1, 1\}$ in the coupled basis $\{|\uparrow\uparrow\rangle, |\uparrow\downarrow\rangle, |\downarrow\uparrow\rangle, |\downarrow\downarrow\rangle\}$, and the ideal Hamiltonian is

$$H^{m,2} = -\frac{\omega}{2} \sum_{j=1,2} Z_j + \frac{J}{4}Z_1 Z_2 - \sum_{i \in \{m\}} \frac{\omega_i}{2} Z_i. \quad (\text{B14})$$

Noticing that the two target qubits are on resonance and decoupled from any other spectators, the Hamiltonian in the rotating frame, with all local spins, therefore becomes

$$H_{\text{rot}}^{m,2} = \frac{J}{4}Z_1 Z_2. \quad (\text{B15})$$

Eventually, the overall error term of the Hamiltonian for this system, including the spectators, is

$$H_{\text{pert}}^{m,2} = \sum_{j \in m, 2} \delta_j Z_j + \sum_{i \in \{m\}, j=1,2} \frac{J_{res}}{4} Z_i Z_j. \quad (\text{B16})$$

where δ_j are variations in qubit energies, J_{res} are unwanted couplings between targets and spectators, while J is the coupling strength tuned to implement the \sqrt{SWAP} gate.

Section C: More Numerical results and details

Here we demonstrate numerical results to illustrate the role that entanglement plays in both analog simulation of the quantum Ising model with a transverse field (QIMF) and quantum control in the quantum dot model.

1. QIMF models

1D-QIMF.— First, we consider a simple 1-D QIMF with Hamiltonian

$$H_0 = h_x \sum_{i=1}^N X_i + h_y \sum_{i=1}^N Y_i + J \sum_i X_i X_{i+1}, \quad (\text{C1})$$

where the parameters $h_x = 0.809, h_y = 0.9045, J = 1$. There is a perturbation term in actual analog simulation $H_{\text{analog}} = H_0 + H_{\text{dis}} + H_{\text{pert}}$. The source of perturbation includes stochastic disorder and intrinsic control imperfections. In our numerical tests, the disorder term H_{dis} is set as a combination of N single-qubit Pauli operators X_i 's, i.e., $H_{\text{dis}} = \sum_{i=1}^N \delta_i X_i$, where δ_i is randomly chosen with respect to a normal distribution and X_i represents Pauli X acting on the i th qubit. The control disorder term is set as $H_{\text{imp}} = \eta \sum_{i=1}^{N-1} X_i X_{i+1}$, where η is a constant. We demonstrate numerical tests of three different scenarios: with disorder only ($\delta_i \in \mathcal{N}(0, 0.001), \eta = 0$), with imperfection only ($\delta_i = 0, \forall i$ and $\eta = 0.001$), and with both disorder and imperfection terms ($\delta_i \in \mathcal{N}(0, 0.001), \eta = 0.001$). We compare the simulation error, defined as

$$\|e^{-iH_{\text{analog}}t} |\psi(0)\rangle - e^{-iH_0 t} |\psi(0)\rangle\|,$$

for a typical initial state versus an atypical initial state in Figure 9. In typical cases ($|\psi(0)\rangle = |0\rangle^{\otimes N}$), entanglement entropy increases with the evolution until saturation, whereas in atypical cases ($|\psi(0)\rangle = |+\rangle^{\otimes N}$), it remains at a low level (See Figure 9(b)(d)(e)). Consequently, in typical scenarios, the simulation error rapidly decreases and stabilizes near the average estimate, whereas in atypical scenarios, the error remains larger and may approach the worst-case estimate given by the spectral norm.

In practical experimental scenarios, the disorder term will include the effects of various perturbations, so it is more reasonable to treat the coefficient of the disorder term as a normally distributed random number $\delta_k \in \mathcal{N}(0, \sigma)$. In our numerical tests, the variance is chosen as $\sigma = 0.001$. And we consider an analog Hamiltonian

$$H' = H_0 + \sum_{k=1}^N \delta_k X_k + \eta \sum_{i=1}^{N-1} X_i X_{i+1}, \quad (\text{C2})$$

where $\eta = 0.001$. In this setting, the analog simulation error is shown to be small for most cases.

2D lattice QIMF model.— We also numerically test a QIMF model on a 4×3 2D spin lattice with Hamiltonian

$$H_0 = h_x \sum_i X_i + h_y \sum_i Y_i + J \sum_{\langle i,j \rangle} X_i X_j, \quad (\text{C3})$$

where $\langle i, j \rangle$ represents an index pair of two nearest-neighbor spins, parameters $h_x = 0.809, h_y = 0.9045, J = 1$. We also consider error models including stochastic disorder and control imperfection terms (see Figure 10).

2. Fermi-Hubbard Model

The Fermi-Hubbard model is fundamental in condensed matter physics, used to describe interacting fermions on a lattice. The Hamiltonian of the 1D Fermi-Hubbard model

$$H_0 = - \sum_{i=1}^L \sum_{\sigma} (a_{i,\sigma}^\dagger a_{i+1,\sigma} + \text{H.c.}) + V \sum_{i=1}^L a_{i,\uparrow}^\dagger a_{i,\uparrow} a_{i,\downarrow}^\dagger a_{i,\downarrow}, \quad (\text{C4})$$

captures the competition between the kinetic energy (with parameter t) of electrons and the on-site Coulomb repulsion (with parameter V). This simple yet rich model helps explain key phenomena such as magnetism, metal-insulator

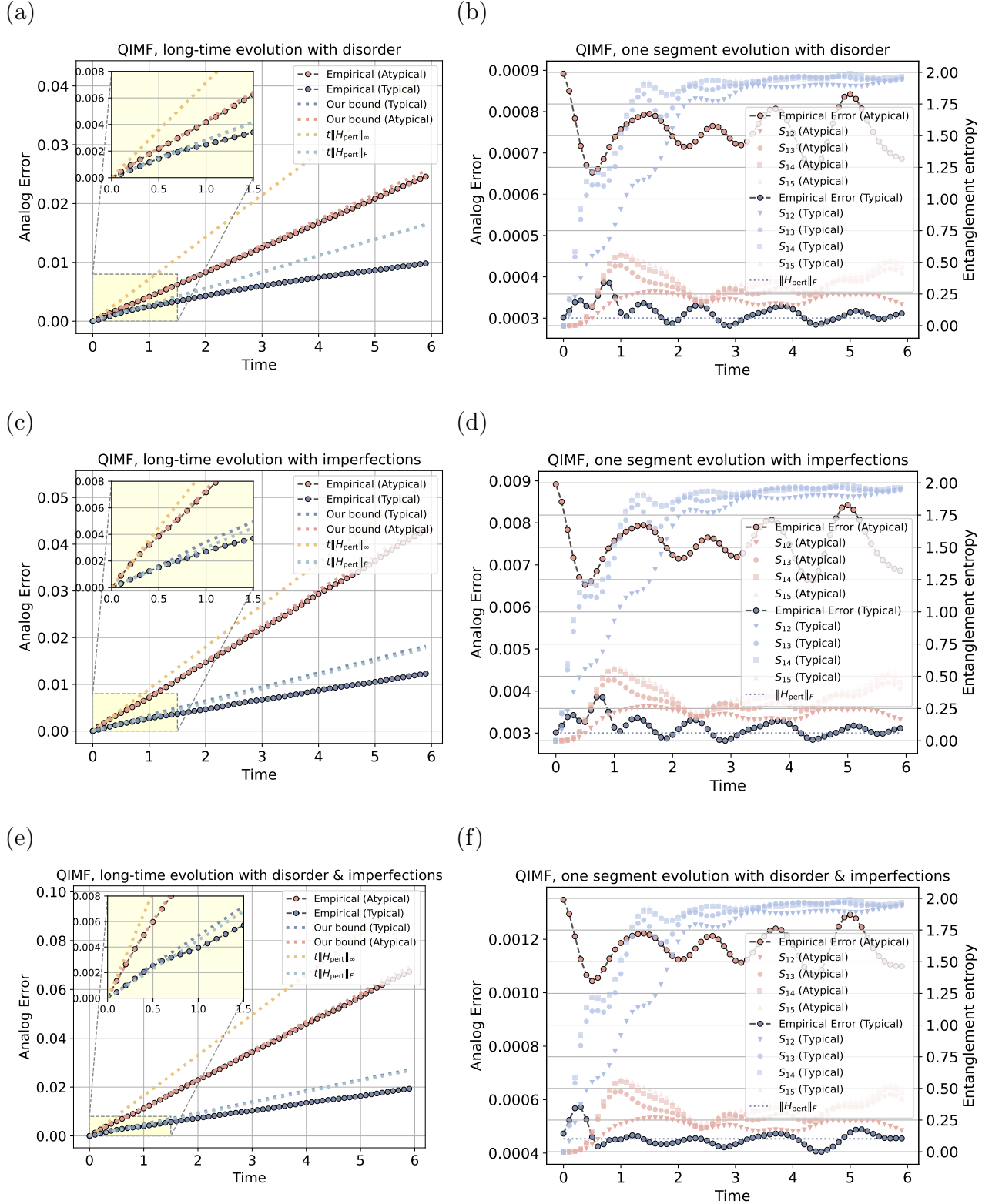


FIG. 9: Error of Analog simulation in typical and atypical cases for 1D QIMF model. (a)(c)(e) Error of long-time analog simulation defined by the distance between real state and simulated state $\|(U_0(t) - U(t))|\psi\rangle\|$. Error models are with disorder only ($\delta_i \in \mathcal{N}(0, 0.01), \eta = 0$), with imperfection only ($\delta_i = 0, \forall i$ and $\eta = 0.01$) and with both disorder and imperfection terms ($\delta_i \in \mathcal{N}(0, 0.01), \eta = 0.01$), respectively. In typical input state, where the entanglement entropy grows during the system's evolution, our estimate closely matches the average-case performance, scaling with $\|H_{\text{pert}}\|_F$. In contrast, in an atypical input state, where the entanglement entropy remains low throughout the evolution, the error scaling deviates significantly from the average case and approaches the worst-case bound characterized by the spectral norm. (b)(d)(f) Error of one-segment analog simulation with respect to different initial states defined as $\|(U_0(\delta t) - U(\delta t))|\psi(t)\rangle\|$. Error models are with disorder only, with imperfection only, and with both disorder and imperfection, respectively. The entanglement entropy of both typical and atypical cases defined on the subsystem of two qubits ($S_{1,2}, S_{1,3}, S_{1,4}, S_{1,5}$) is also shown.

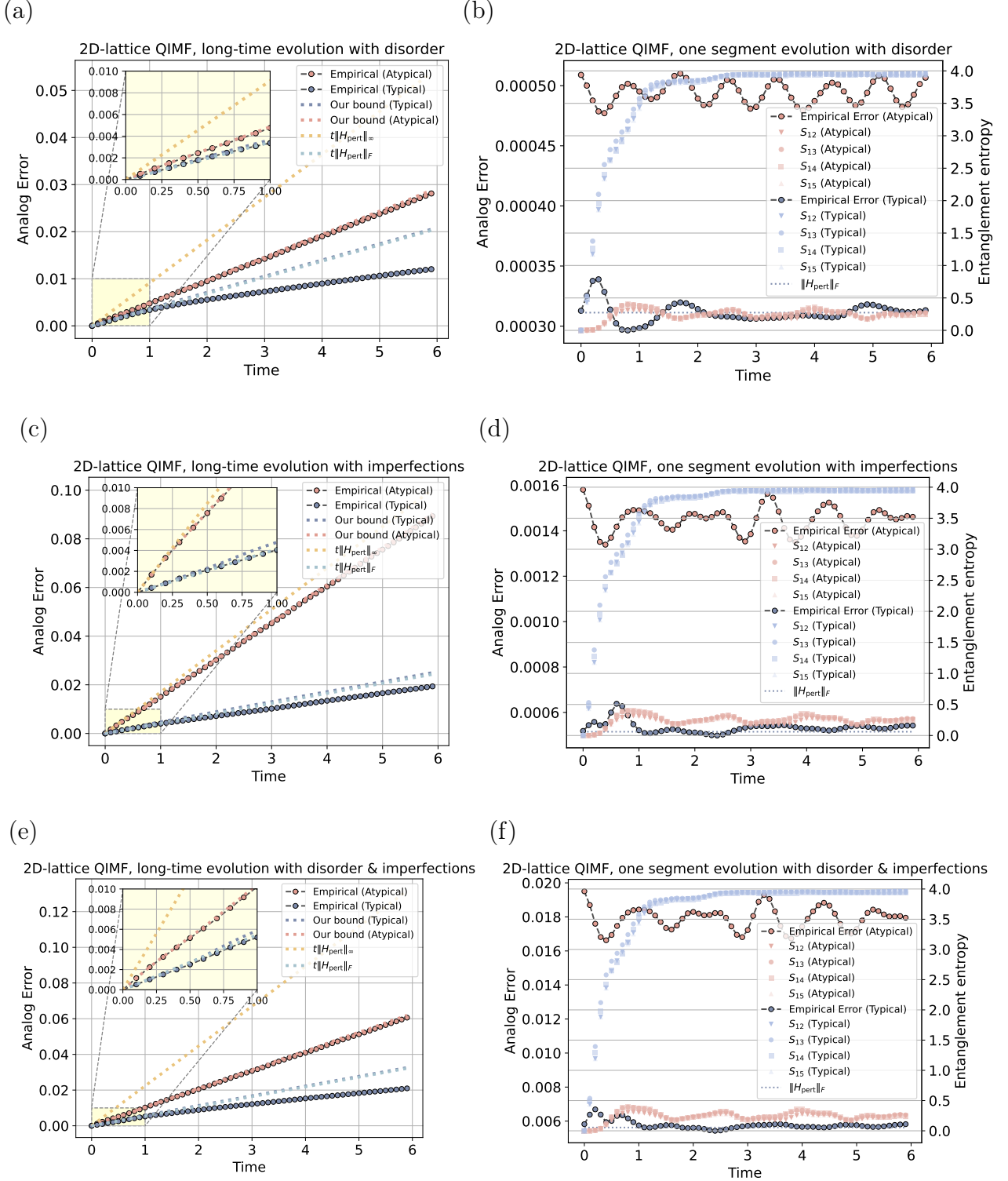


FIG. 10: Error of Analog simulation in typical and atypical cases for 2D QIMF model. (a)(c)(e) Error of long-time analog simulation defined by the distance between real state and simulated state $\|(U_0(t) - U(t))|\psi\rangle\|$. Error models are with disorder only ($\delta \in \mathcal{N}(0, 0.001), \eta = 0$), with imperfection only ($\delta = 0, \eta = 0.001$), and with both disorder and imperfection ($\delta \in \mathcal{N}(0, 0.001), \eta = 0.001$), respectively. In typical input state, where the entanglement entropy grows during the system's evolution, our estimate closely matches the average-case performance, scaling with $\|H_{\text{pert}}\|$. In contrast, in an atypical input state, where the entanglement entropy remains low throughout the evolution, the error scaling deviates significantly from the average case and approaches the worst-case bound characterized by the spectral norm. (b)(d)(f) Error of one-segment analog simulation with respect to different initial states defined as $\|(U_0(\delta t) - U(\delta t))|\psi(t)\rangle\|$. Error models are with disorder only, with imperfection only, and with both disorder and imperfection, respectively. The entanglement entropy of both typical and atypical cases defined on the subsystem of two qubits ($S_{1,2}, S_{1,3}, S_{1,4}, S_{1,5}$) is also shown.

RCPs	Ω_m (MHz)	T (ns)	a	ϕ
X_π	150	180	[0.2374, 0.2683, 0.1459, 0.0335, 0.0030, 0.0144]	[-0.0055, -0.0021, -0.0006, -0.2457, -0.0157]
$X_{\pi/2}$	150	180	[0.1735, 0.1438, 0.0625, -0.0427, -0.0606, 0.0207]	[0.0013, 0.0049, -0.0139, -0.0093, 0.0062]
$X_{2\pi}$	150	180	[0.1522, 0.1288, 0.0434, -0.0866, -0.0375, -0.0174]	[0.0093, -0.0431, 0.0567, -0.0104, -0.0313]

TABLE I: Optimized pulse parameters for different RCPs.

transitions, and high-temperature superconductivity. Fermionic systems are characterized by anticommutation relations between creation and annihilation operators, expressed as

$$\{a_i, a_j^\dagger\} = \delta_{ij}, \quad \{a_i, a_j\} = \{a_i^\dagger, a_j^\dagger\} = 0. \quad (\text{C5})$$

However, quantum computers operate on qubits that obey commutation rather than anticommutation relations. To simulate fermions on qubits, one uses transformations such as the Jordan–Wigner (JW) transform, which maps fermionic operators to strings of Pauli matrices:

$$a_j = (\otimes_{k<j} Z_k) \otimes \frac{X_j + iY_j}{2}, \quad a_j^\dagger = (\otimes_{k<j} Z_k) \otimes \frac{X_j - iY_j}{2}. \quad (\text{C6})$$

In our numerical tests, we consider simulating a Fermi-Hubbard model with parameters $t = 1$ and $U = 0.5$. Compared to the Hamiltonian H_0 of the target free fermion model, the Hamiltonian of the simulator H_{analog} contains an additional noise term from the Coulomb potential.

$$H_0 = - \sum_{i=1}^{L-1} (c_j^\dagger c_{j+1} + c_{j+1}^\dagger c_j), \quad (\text{C7})$$

$$H_{\text{pert}} = \delta \sum_{i=1}^L a_{i,\uparrow}^\dagger a_{i,\uparrow} a_{i,\downarrow}^\dagger a_{i,\downarrow}, \quad (\text{C8})$$

$$H_{\text{analog}} = H_0 + H_{\text{pert}}. \quad (\text{C9})$$

3. Entanglement-induced resilience in quantum control

In the main text, we demonstrate the relationship between the effective error of a single-qubit gate with robust control pulses (RCPs) and entanglement entropy in a 2D lattice. The RCPs used in the main text is given by Ref. [55] and take the form

$$\Omega(t) = \Omega_m \sin(\pi t/T) (a_0 + \sum_{j=1}^n a_j \cos(2\pi j t/T + \phi_j)), \quad (\text{C10})$$

where parameters are listed in Table I.

Here, we demonstrate a 2-qubit case where the implementation of a 2-qubit gate produces disturbances on 6 neighboring qubits. We consider the Hamiltonian given by Eq. (B15) with $J = 10\pi$ MHz and perturbation Eq. (B16) with parameters $\delta = 100$ kHz, $J_{\text{residue}} = 100$ kHz. The numerical results are demonstrated in Figure 11. To illustrate the relationship between error and the entanglement entropy between subsystem of the 8 involved qubits and its complementary subsystem, we prepare a set of purified Gibbs states

$$|\psi_T\rangle_{AB} = \frac{\sum_i e^{-\epsilon_i/T} |\phi_i\rangle_A |\phi_i^*\rangle_B}{\|\sum_i e^{-\epsilon_i/T} |\phi_i\rangle_A |\phi_i^*\rangle_B\|}, \quad (\text{C11})$$

where A denotes the system composed of the evolved, the remaining system B includes the other 8 qubits. $\{(\epsilon_i, |\phi_i\rangle_A)\}$'s represent eigenvalues and eigenvectors of Hamiltonian $V = -\sum_{i \in A} Z_i$, and $|\phi_i^*\rangle_B$'s are corresponding states on B .

The reduced density matrix of the purified Gibbs state is

$$\rho_A = \text{tr}_B(|\psi_T\rangle\langle\psi_T|) = \frac{1}{\mathcal{Z}} \sum_i e^{-2\epsilon_i/T} |\phi_i\rangle\langle\phi_i|, \quad (\text{C12})$$

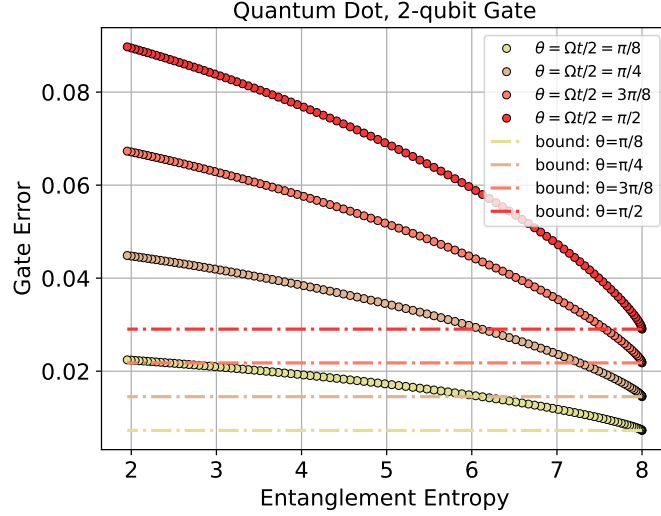


FIG. 11: Implementing a 2-qubit gate, the gate error versus entanglement entropy. States are chosen according to Eq. (C11), where temperatures are chosen to be $T \in \{\frac{1}{i} | t \in \{0.008, 0.016, \dots, 0.48\}\}$. The entanglement entropy is calculated with respect to the subsystem of the first two qubits. When the entanglement entropy gets close to its maximum $\log d = 2$, the gate error quickly reduces to the bound given by Eq (15). The dependence of gate error on entropy is well described by a biquadratic root function, which is consistent with the entanglement-based bound with a maximally entangled state.

where $\mathcal{Z} = \sum_i e^{-2\epsilon_i/T}$. So the entanglement entropy defined by the von Neumann entropy is

$$S_A = -\text{tr}(\rho_A \ln \rho_A) = \frac{1}{\mathcal{Z}} \sum_i \frac{2\epsilon_i}{T} e^{-2\epsilon_i/T} |\phi_i\rangle \langle \phi_i|. \quad (\text{C13})$$

And the gate error can be calculated by

$$\|(U - U_0) |\psi_T\rangle\| = \text{tr}[(U - U_0)^\dagger (U - U_0) |\psi_T\rangle \langle \psi_T|] = \text{tr}_A \{ \text{tr}_B [(U - U_0)^\dagger (U - U_0)] \rho_A \} \quad (\text{C14})$$

We consider the implementation of a 2-qubit gate with perturbation Hamiltonian given by Eq. (B13) with gate time $T = 25\text{ns}, 50\text{ns}, 75\text{ns}, 100\text{ns}$, respectively.

Section D: Entanglement-induced resilience in quantum circuits

Suppose a coherent noise model satisfying $U = U_0 e^{-i\lambda E}$, where U_0 is the ideal evolution and $e^{-i\lambda E}$ is the error unitary. The p -order product formula of Trotterization is the special case of this model. Every single segment of the product formula can be modeled by the proposed model. As we all known, a single (short-time) segment of product formula is given as $\mathcal{U}_p(\delta t) = U_0(\delta t)(I + \mathcal{M})$ where $\|\mathcal{M}\| = \mathcal{O}(\delta t^{p+1})$. Since $I + \mathcal{M}$ is a unitary, one can denote it as $e^{\delta t^{p+1} M} = I + \delta t^{p+1} M + t^{2p+2} M^2/2 \dots = I + \mathcal{M}$. Different from the Trotterization case, the model $U = U_0 e^{-i\lambda E}$ does not assume U_0 is a short-time evolution (close to identity), and it can be a highly nonlocal gate or strong coupling evolution.

In the following, $\|A\|$ denote spectral norm, $\|A|\psi\rangle\| = \sqrt{\langle \psi | A^\dagger A | \psi \rangle}$ denote vector norm. $S(\rho_A) = -\text{Tr}(\rho_A \log \rho_A)$ is defined as the entanglement (Von Neumann) entropy. The entanglement-based lemma for a quantum circuit is given as follows.

Lemma 3 (Entanglement-induced circuit resilience). *Given a quantum state $|\psi\rangle$, an idea unitary/evolution U_0 and a approximate one U with coherent error $e^{-i\lambda E}$ satisfying $U = U_0 e^{-i\lambda E}$ ($E = \sum_j E_j$ is a Hermitian operator), the additive error of evolution is defined as $U - U_0$, and the evolved state is bounded by*

$$\|(U - U_0) |\psi\rangle\| = \mathcal{O}\left(\sqrt{\frac{\text{Tr}(\mathcal{B})}{d}} + \sum_j \sqrt{\|\mathcal{B}_j\| \sqrt{2 \log(d_{\text{supp}}(\mathcal{B}_j)) - 2S(\rho_j)}}\right). \quad (\text{D1})$$

where

$$\mathcal{B} = \sum_{s_1, s_2=1, s_1+s_2=\text{even}}^{s_1+s_2=K+1} \frac{(-1)^{s_2} (i\lambda)^{s_1+s_2} (\sum_{j_1, j_2, \dots, j_{s_1+s_2}}^J \prod_{i=1}^{s_1+s_2} E_{j_i})}{s_1! s_2!},$$

$$\text{and } \mathcal{B}_j = \mathcal{B}_{j(s_1, s_2)} = \frac{(-1)^{s_2} (i\lambda)^{s_1+s_2} (\sum_{j_1, j_2, \dots, j_{s_1+s_2}}^J \prod_{i=1}^{s_1+s_2} E_{j_i})}{s_1! s_2!}.$$

Proof. Set $\mathcal{A} = U - U_0 = U_0(e^{-i\lambda E} - I) = U_0 \sum_{s=1}^{\infty} \frac{(-i\lambda E)^s}{s!}$, one has

$$\mathcal{A}^\dagger \mathcal{A} = \sum_{s_1=1}^{\infty} \left[\frac{(-i\lambda E)^{s_1}}{s_1!} \right]^\dagger \left[\sum_{s_2=1}^{\infty} \frac{(-i\lambda E)^{s_2}}{s_2!} \right]. \quad (\text{D2})$$

Since $e^{-i\lambda E}$ is an error unitary, and generally should be a perturbative rotation with some specific Hermitian operator E , where $E = \sum_j E_j$ and each E_j is local (with constant weight or support). For example, a two-qubit gate or interaction evolution, its perturbation unitary is local because its driving Hamiltonian is local.

Here λ is a small parameter, we truncated the additive error up to K order of λ , so that

$$\mathcal{A} = U_0 \left[\sum_{s=1}^K \frac{(-i\lambda E)^s}{s!} + \mathcal{O}(\lambda^{K+1}) \right].$$

Now the positive semi-definite operator $\mathcal{A}^\dagger \mathcal{A}$ (leading term up to $K+1$ order) is given as

$$\begin{aligned} \mathcal{A}^\dagger \mathcal{A} &= \left[\sum_{s_1=1}^K \frac{(-i\lambda E)^{s_1}}{s_1!} + \mathcal{O}(\lambda^{K+1}) \right]^\dagger \left[\sum_{s_2=1}^K \frac{(-i\lambda E)^{s_2}}{s_2!} + \mathcal{O}(\lambda^{K+1}) \right] \\ &= \sum_{s_1, s_2=1}^{s_1+s_2=K+1} \frac{(-1)^{s_2} (i\lambda E)^{s_1+s_2}}{s_1! s_2!} + \mathcal{O}(\lambda^{K+2}) \\ &= \sum_{s_1, s_2=1, s_1+s_2=\text{even}}^{s_1+s_2=K+1} \frac{(-1)^{s_2} (i\lambda E)^{s_1+s_2}}{s_1! s_2!} + \mathcal{O}(\lambda^{K+2}) \\ &= \sum_{s_1, s_2=1, s_1+s_2=\text{even}}^{s_1+s_2=K+1} \frac{(-1)^{s_2} (i\lambda)^{s_1+s_2} (\sum_{j_1, j_2, \dots, j_{s_1+s_2}}^J \prod_{i=1}^{s_1+s_2} E_{j_i})}{s_1! s_2!} + \mathcal{O}(\lambda^{K+2}). \end{aligned} \quad (\text{D3})$$

For simplicity, set $\mathcal{A}^\dagger \mathcal{A} = \mathcal{B} + \mathcal{O}(\lambda^{K+2}) = \sum_j \mathcal{B}_j + \mathcal{O}(\lambda^{K+2})$ where $\mathcal{B}_j = \mathcal{B}_{j(s_1, s_2)} = \frac{(-1)^{s_2} (i\lambda)^{s_1+s_2} (\sum_{j_1, j_2, \dots, j_{s_1+s_2}}^J \prod_{i=1}^{s_1+s_2} E_{j_i})}{s_1! s_2!}$.

Using the Lemma 4 below, we have

$$\|(U - U_0) |\psi\rangle\| = \mathcal{O}\left(\sqrt{\frac{\text{Tr}(\mathcal{B})}{d}}\right) + \sum_j \sqrt{\|\mathcal{B}_j\| \sqrt{2 \log(d_{\text{supp}(\mathcal{B}_j)}) - 2S(\rho_j)}}. \quad (\text{D4})$$

□

Corollary 2 (1-order approximation). *Given approximate unitary $U = U_0 e^{-i\lambda E}$ where U_0 is the ideal one, for truncated order $K = 1$, the additive error $\mathcal{A} = U - U_0 = U_0(-i\lambda E + \mathcal{O}(\lambda^2))$ resulting $\mathcal{A}^\dagger \mathcal{A} = \lambda^2 E^2 + \mathcal{O}(\lambda^3) = \lambda^2 \sum_{j, j'} E_j E_{j'} + \mathcal{O}(\lambda^3)$. For any quantum state $|\psi\rangle$, the additive error $\|\mathcal{A} |\psi\rangle\| = \|(U - U_0) |\psi\rangle\|$ is bounded by*

$$\|(U - U_0) |\psi\rangle\| = \mathcal{O}(\lambda \|E\|_F) + \lambda \sum_j \sqrt{\|E_j E_{j'}\| \sqrt{2 \log(d_{\text{supp}(E_j E_{j'})}) - 2S(\rho_j)}}, \quad (\text{D5})$$

where $\|A\|_F^2 := \text{Tr}(A^\dagger A)/d$ is the (square) of the normalized Frobenius norm, $\rho_j := \text{Tr}_{[N] \setminus \text{supp}(A_j)}(|\psi\rangle \langle \psi|)$ is the reduced density matrix of $|\psi\rangle \langle \psi|$ on the subsystem of $\text{supp}(A_j)$, and $S(\rho_j)$ is the entanglement entropy of ρ_j .

Corollary 3 (2-order approximation). *Given approximate unitary $U = U_0 e^{-i\lambda E}$ where U_0 is the ideal one, for truncated order $K = 2$, the additive error $\mathcal{A} = U - U_0 = U_0(-i\lambda E - \frac{\lambda^2 E^2}{2} + \mathcal{O}(\lambda^3))$ resulting*

$$\mathcal{A}^\dagger \mathcal{A} = \lambda^2 E^2 - \frac{-i\lambda^3 E^3 + i\lambda^3 E^3}{2} + \mathcal{O}(\lambda^4) = \lambda^2 E^2 + \mathcal{O}(\lambda^4).$$

For any quantum state $|\psi\rangle$, the additive error $\|\mathcal{A}|\psi\rangle\| = \|(U - U_0)|\psi\rangle\|$ is bounded by

$$\|U - U_0|\psi\rangle\| = \mathcal{O}(\lambda\|E\|_F) + \lambda \sum_{j,j'} \sqrt{\|E_j E_{j'}\| \sqrt{2 \log(d_{\text{supp}(E_j E_{j'})}) - 2S(\rho_j)}}, \quad (\text{D6})$$

where $\|A\|_F^2 := \text{Tr}(A^\dagger A)/d$ is the (square) of the normalized Frobenius norm, $\rho_j := \text{Tr}_{[N] \setminus \text{supp}(A_j)}(|\psi\rangle\langle\psi|)$ is the reduced density matrix of $|\psi\rangle\langle\psi|$ on the subsystem of $\text{supp}(A_j)$, and $S(\rho_j)$ is the entanglement entropy of ρ_j .

Note that $\text{Tr}(E^2)/d = \|E\|_F$ since $E^\dagger = E$. It can be seen that the additive error $\|\mathcal{A}|\psi\rangle\|$ of 1-order and 2-order approximation of $e^{-i\lambda E}$ is the same while ignoring the higher-order error terms.

Since the unitary here is not a short-time evolution, i.e., U_0 is far from I and can be highly nonlocal, $\mathcal{A} = U_0(e^{-i\lambda E} - I)$ is not local anymore. Fortunately, $\mathcal{A}^\dagger \mathcal{A}$ can be local. Now one can simply rewrite the Lemma proposed in [22], obtaining

Lemma 4. [22] *Let $A = \sum_j A_j$ be a positive semi-defined operator, acting on N qubits, where A_j acts nontrivially on the subsystem with $\text{supp}(A_j)$. Then*

$$|\langle\psi|A|\psi\rangle| \leq \frac{\text{Tr}(A)}{d} + \sum_j \|A_j\| \sqrt{2 \log(d_{\text{supp}(A_j)}) - 2S(\rho_j)}, \quad (\text{D7})$$

where $\rho_j := \text{Tr}_{[N] \setminus \text{supp}(A_j)}(|\psi\rangle\langle\psi|)$ is the reduced density matrix of $|\psi\rangle\langle\psi|$ on the subsystem of $\text{supp}(A_j)$, and $S(\rho_j)$ is the entanglement entropy of ρ_j .

Proof. The term A_j in the expression for A only acts nontrivially on $\text{supp}(A_j)$. We denote its nontrivial part by $L_j := \text{Tr}_{[N] \setminus \text{supp}(A_j)}(A_j)$. Since $2^{-N} \text{Tr}(A_j) = d_{\text{supp}(A_j)}^{-1} \text{Tr}(L_j)$, we have

$$\begin{aligned} \sum_j \langle\psi|A_j|\psi\rangle &= \sum_j \text{Tr}(L_j \rho_j) = \text{Tr}[L_j(\rho_j - \mathbb{I}_{\text{supp}(A_j)}/d_{\text{supp}(A_j)})] + \sum_j \text{Tr}(L_j)/d_{\text{supp}(A_j)} \\ &= \sum_j \text{Tr}[L_j(\rho_j - \mathbb{I}_{\text{supp}(A_j)}/d_{\text{supp}(A_j)})] + \text{Tr}(A_j)/2^N \\ \sum_j &\leq \|L_j\| \text{Tr}|\rho_j - \mathbb{I}_{\text{supp}(A_j)}/d_{\text{supp}(A_j)}| + \sum_j \text{Tr}(A_j)/2^N \\ &= \sum_j \|A_j\| \text{Tr}|\rho_j - \mathbb{I}_{\text{supp}(A_j)}/d_{\text{supp}(A_j)}| + \text{Tr}(A)/2^N. \end{aligned} \quad (\text{D8})$$

Moreover, the trace distance of ρ_j and $\mathbb{I}_{\text{supp}(A_j)}/d_{\text{supp}(A_j)}$ can be bounded by the relative entropy, the quantum Pinsker inequality, as

$$\text{Tr}|\rho_j - \mathbb{I}_{\text{supp}(A_j)}/d_{\text{supp}(A_j)}| \leq \sqrt{2S(\rho_j \|\mathbb{I}_{\text{supp}(A_j)}/d_{\text{supp}(A_j)})} = \sqrt{2 \log(d_{\text{supp}(A_j)}) - 2S(\rho_j)}. \quad (\text{D9})$$

□

If $A = B^\dagger B$, where B is a square matrix, Lemma 4 reduces to the one in [22].